

# Design of Hydrofoil for the Resistance Improvement of Planing Boat Based on CFD Technology

Hailong Shen<sup>a,b</sup>, Qing Xiao<sup>b</sup>, Jin Zhou<sup>a</sup>, Yumin Su<sup>a</sup>, Xiaosheng Bi<sup>a,\*</sup>

<sup>a</sup> Science and Technology on Underwater Vehicle Technology Laboratory, Harbin Engineering University, Harbin, PR China

<sup>b</sup> Department of Naval Architecture, Ocean and Marine Engineering, University of Strathclyde, Glasgow, U.K

**Abstract.** The purpose of this study was to design a hydrofoil which would improve boat performance through enhanced resistance reduction. Commercial CFD code STARCCM+ was used to solve the Unsteady Reynolds Averaged Navier Stokes Equations for the flow around the boat. Uncertainty study is conducted in order to obtain an effective and reliable numerical calculation method. The method was then validated by direct comparison of the numerical data at different speeds with the test data of USV01 planing boats. Accordingly, twelve hydrofoil design cases were considered, and their resistance reduction performance at 8m/s was predicted and compared with each other through the numerical calculation method. Effects of hydrofoil parameters such as longitudinal installation position, span, attack angle, installation height on the resistance reduction performance were investigated. One of 12 cases was chosen to investigate the resistance reduction effect of hydrofoil at different speeds. The results show that the hydrofoil, with proper installation position and design parameters, has a significant resistance reduction effect. At 8m/s, the hydrofoil designed in this paper can reduce boat resistance by up to 30.74%. To analyze the principle of hydrofoil, the flow field around hull and hydrofoil was numerically simulated and studied.

**Key words:** planing boat; CFD; resistance performance; Hydrofoil resistance reduction; sailing attitude; overset grid

## 1. Introduction

As a high-performance vessel, the planing boat has a wide range of application such as boat racing, recreation, military operations, transportation among others. Hence, research on the planing boat has been developing continuously for many years. In the earlier studies, the design and hydrodynamic performance prediction of planing boat was carried out on the basis of model tests. Savitsky, Clement and Blount carried out the most famous and representative models tests.

Daniel Savitsky (1964) conducted a research for about 40 years on the hydrodynamics of planing surfaces through a series of flat plates and prismatic surface model tests. Based on the research, the first practical method of determining; the lift, resistance and the dynamic equilibrium of planing hulls, with reasonable precision, was proposed. Clement and Blount (1963) performed extensive models tests to obtain the resistance of the series 62 and 65 models with a range of deadrise angles. The-presented experimental data on these planing hulls became a valuable database for subsequent studies. Afterwards, many model test experiments were conducted. Yousefi et al. (2013) contributed major experimental investigations on planing hulls and a summary of results obtained is widely cited. Recently, various researches have been carried out through model tests.

Although experiments are the most reliable and widely accepted means for modeling the flows around planing hulls, they are expensive and time consuming. Furthermore, the data obtained is only valid for a limited set of conditions. Please note that in order to meet the design specifications requirement, a series of model tests are required. This highlights a further drawback in the form of the lengthy

\*Corresponding author: Xiaosheng Bi.

E-mail address: bixiaosheng@hrbeu.edu.cn.

design cycle of the new planing boats. The inherent limitations of analytical and experimental

techniques have motivated the researchers to use computational fluid dynamics (CFD) methods to study planing hulls in recent years.

In general, there are many computational approaches for hydrodynamic analysis of planing hulls. These methods are broadly classified as potential theory method and viscous flow theory method. Potential theory method involve solution of transport equations for invicid flow. On the other hand, in viscous flow method, the flow is modelled by the Navier Stokes equation. Navier Stokes equation are a set of differential equations, solved by numerical discretization. According to [Yousefi et al. \(2013\)](#) numerical methods are grouped into four types namely; Boundary Element Method, Finite Volume Method, Finite Difference Method and Finite Element method. Among them, Finite Volume Method is the dominant method for planing hulls and is more popular. [H. Ghassemi et al. \(2008\)](#), [A.R. Kohansal et al. \(2010\)](#) and [K.I. Matveev \(2014, 2015\)](#) implemented potential theory to solve the invicid flow around the planing hull and obtained faster results. [S.M. Mousaviraad \(2015\)](#), [P. Lotfi \(2015\)](#) and [S.T.G. Veysi \(2015\)](#) used Unsteady Reynolds-Averaged Navier Stokes Equations (URANS) to solve the viscous and transient flow. Viscous methods have been found to be more accurate and reliable though they consume considerably amount of time.

The recent past has witnessed continued development in computational techniques and improvement of commercial CFD software reliability in recent years, CFD. As a result, there has been a wide application of commercial CFD software. ([Brizzolara and Serra, 2011](#); [Jahanbakhsh et al., 2009](#); [Seif et al., 2009](#); [Senocak and Iaccarino, 2005](#)). [Yi Jiang et al. \(2017\)](#) used the Finite Volume Method (FVM) based software CFX to simulate the tunnel flow and the forward motion of planing trimaran in calm water. [H.K. Moghadam et al. \(2015\)](#) numerically simulated the forward motion for a series of tunneled planing hulls with different tunnel aperture using FLUENT. Their results showed that the small tunnel aperture could achieve more resistance reduction at high Froude numbers. Based on CFD, [Hosseini A. \(2020\)](#) carried out performance prediction of a planing hull in a calm-water condition. The aim was to evaluate similarities and differences between results by different CFD models. They recommend combination of the morphing and DES models during CFD modeling of a planing hull at high-speeds. [Tavakoli S et al. \(2020\)](#) used different approaches to investigate the unsteady planning motion in waves. The study was conducted through towing tank tests, CFD, and the 2D + t model. The analysis shows that all motions can be nonlinear despite the fact that CFD and 2D + t model may predict weaker nonlinear behavior at higher speed.

[Agostino De Marco et al. \(2017\)](#) performed numerical hydrodynamic analysis of a stepped planing hull using the  $k-\omega$  shear stress transport (SST) turbulence model. [Lotfi et al. \(2015\)](#) used an unsteady RANS solver (ANSYS-CFX) based on a Volume of Fluid (VoF) approach to examine the characteristics and performance of a planing hull having one transverse step. [Niazmand bilandi et al. \(2020,2021\)](#) proposed a numerical method based on 2D+T theory for performance prediction of heeled double-stepped planing hull. They also used a CFD model to simulate the unsteady motion of the double-stepped boats in waves. It is evident that CFD has become a fundamental tool for hydrodynamic investigations. This is attributed to its ability to perform detailed analysis and to reduce the number of costly towing tank tests. Nevertheless, the results of hydrodynamic experiment are always necessary alongside and are required during validation of numerical results.

From literature, the primary objective of researchers on planning hull is to reduce the resistance and enhance the stability and sea-keeping performance. It is obvious that many effective methods to improve the performance of planing hulls have been implemented. For instance, appendages similar to spray rails have been applied to planing hulls to reduce trim and resistance, and increase longitudinal and transverse stability ([Yousefetal, 2013](#); [Larsson et al., 2014](#)). According to findings by [Clement \(1964\)](#), the optimal location of spray rails varies with the hull geometry whereas the flow stagnation lines varies with spray location. [S. Bal \(2003, 2007\)](#) studied the influence of high-speed, surface-piercing hydrofoils on the performance of planing hull. [Lee et al. \(2005\)](#) tried to improve the

resistance performance of high-speed vessels by appendage for 50 knots class planing hull form. Stepped hull configuration was used to reduce the resistance of planing hull (Agostino De Marco et al., 2017; D. Savitsky et al., 2010; K.I. Matveev, 2012; P. Lotfi, M et al., 2015).

Migeotte G et al. (1997) selected the suitable foil assist systems for the semi-displacement hulls. The results presented showed that the hydrofoil assistance was advantageous on catamarans performance. Chi Yungpeng et al. (1995,1996) conducted a study on resistance and seakeeping of high-speed channel craft with hydrofoils. The study involved a series of experiments of channel craft with hydrofoils and stern wave suppression plate. The average resistance reduction of about 16% was achieved compared to the conventional channel craft. Sclavounos et al. (2014) studied the influence of bow hydrofoil on the hydrodynamic performance of ship. They also considered the effect of the hydrofoil parameters and working conditions on drag reduction. Budiyanto M A. (2019,2020) investigated the application of stern foil on a patrol boat and a multi-chine hull through experiment and numerical methods. They were able to select the suitable position and foil shape. They found out that the stern foil and multi-chine hull could achieve up to 26.705% and 41.2% resistance reduction respectively. Azis D N et al. (2019) recorded about 61.5 % reduction of the catamaran's effective Horsepower (EHP) when two hydrofoils were installed at the bottom of catamaran. Haekal Dwiputera et al. (2020) studied the resistance reduction performance of the stern hydrofoil at different angles of attack. They found that when the Froude number was in the range of 0.5-0.75, a specific stern hydrofoil effectively reduced the resistance by 9%-26%. Hou Hongbo et al. (2020) through model tests studied a hydrofoil installed behind the stern. Compared with no hydrofoil, the total drag coefficient dropped by 6.4%. In the wave experiment, the hydrofoil greatly improved the seakeeping of the model. Ismail I N et al. (2020) compared the resistance reduction effects of different types of hydrofoils. It was noted that the type and shape of hydrofoils have a great influence on ship resistance. The rectangular fully submerged hydrofoil gave the highest resistance reduction of up to 17.82%.

In this work, a CFD approach is used to investigate the resistance reduction effect of the hydrofoil on planing boat. Grid convergence study was carried in order to obtain a reliable and verifiable numerical prediction method. Based on the USV01 planing model test data, the numerical calculation method was further validated. A new hydrofoil model of planing boat was proposed followed by parametric optimization. Firstly, the influence of hydrofoil longitudinal position on planing boat resistance reduction was studied. Then, based on the selected hydrofoil installation position, the effects of span, angle of attack and installation height on the hydrodynamic of the planing boat were investigated. Please note that all numerical simulations were performed for a planing hull appended with fixed hydrofoil in calm water.

## 2. Governing equations and Turbulence model

### 2.1 Governing equations

The fluid is assumed to be viscous and incompressible. Under isothermal conditions, conservation of mass and momentum conservation equations of unsteady incompressible viscous flow can be expressed as:

$$\frac{\partial}{\partial t} \int_V \rho dV + \int_S \rho (\vec{U} - \vec{U}_a) \cdot \vec{n} dS = 0 \quad (1)$$

$$\frac{\partial}{\partial t} \int_V \rho U_i dV + \int_S \rho U_i (\vec{U} - \vec{U}_a) \cdot \vec{n} dS = \int_S (\tau_{ij} I_j - p I_i) \cdot \vec{n} dS + \int_V \rho g_i dV \quad (2)$$

Where;  $t$  is time,  $\rho$  is density,  $V$  is control volume bounded by the closed surface  $S$  moving at the velocity  $\vec{U}_a$  with a unit normal vector  $\vec{n}$  directed outward.  $\vec{U}$  and  $p$  represent the velocity and

pressure fields respectively,  $\tau_{ij}$  and  $g_i$  are the components of the viscous stress tensor and the gravity vector,  $U_i$  is the components of the velocity on  $x_i$  axis,  $I_i$  and  $I_j$  are direction vectors.

Nichols and Hirt (1981) proposed VOF method for solving the two-phase flow. The basic principle of VOF method is to calculate the volume ratio function  $F$  between a fluid and the grid in the grid element in order to determine the interface of two-phase flow. The function  $F$  satisfies the following differential equation:

$$\frac{\partial F}{\partial t} + u \frac{\partial F}{\partial x} + v \frac{\partial F}{\partial y} + w \frac{\partial F}{\partial z} = 0 \quad (3)$$

where  $u$ ,  $v$  and  $w$  are the velocity components.

In this research, the motion equations of force and moment equilibrium were adopted in solving for the two degree of freedom motion (pitch and heave) of the planing boat in calm water as follows:

$$\begin{aligned} \vec{F} &= m \frac{d^2 \vec{X}}{dt^2} \\ \vec{M} &= \frac{d}{dt} \left( I \frac{d\vec{\theta}}{dt} \right) \end{aligned} \quad (4)$$

Where  $\vec{X}$  and  $\vec{\theta}$  are the linear and angular displacement respectively.  $I$  is the inertia mass matrix of the hull around the gravity center.

## 2.2 Turbulence model

The SST  $k$ - $\omega$  turbulence model is widely applied in the planing boat hydrodynamic performance prediction (Wang et al., 2014; Jiang et al., 2017; Marco et al., 2017; Agostino De Marco et al., 2017). Here the viscous flows are typically resolved and turbulence models are applied throughout the boundary layer. Similar to the standard  $k$ - $\omega$  model, the transport equations for  $k$  and  $\omega$  are slightly modified as follows (David C. Wilcox, 1994, 2008).

$$\frac{D}{Dt}(\rho k) = \frac{\partial}{\partial x_j} \left[ \left( \mu + \frac{\mu_t}{\sigma_k} \right) \frac{\partial k}{\partial x_j} \right] + \tilde{G}_k - Y_k + S_k \quad (5)$$

$$\frac{D}{Dt}(\rho \omega) = \frac{\partial}{\partial x_j} \left[ \left( \mu + \frac{\mu_t}{\sigma_\omega} \right) \frac{\partial \omega}{\partial x_j} \right] + G_\omega - Y_\omega + D_\omega + S_\omega \quad (6)$$

where  $\tilde{G}_k$  represents the generation of turbulent kinetic energy that arises due to mean velocity gradients,  $G_\omega$  is generation of  $\omega$ , and  $Y_k$  and  $Y_\omega$  represent the dissipation of  $k$  and  $\omega$  due to turbulence.  $\alpha_k$  and  $\alpha_\omega$  are the turbulent Prandtl numbers for  $k$  and  $\omega$  respectively, and  $S_k$  and  $S_\omega$  are source terms defined by the user.  $D_\omega$  is the cross diffusion term.

The turbulent (or eddy) viscosity  $\mu_t$  is computed by

$$\mu_t = \frac{\rho k}{\omega} \frac{1}{\max \left[ \frac{1}{\alpha^*}, \frac{SF_2}{a_1 \omega} \right]} \quad (7)$$

Where  $S$  is the strain rate magnitude and  $\alpha^*$  is the damping coefficient. Unlike the standard model, SST  $k$ - $\omega$  incorporates the blending functions  $F_1$  and  $F_2$  into the Prandtl numbers to ensure that the model equations behave appropriately in both near wall and far field zones.

$$\sigma_k = \frac{1}{\frac{F_1}{\sigma_{k,1}} + \frac{1-F_1}{\sigma_{k,2}}} \quad \sigma_\omega = \frac{1}{\frac{F_1}{\sigma_{\omega,1}} + \frac{1-F_1}{\sigma_{\omega,2}}} \quad (8)$$

Where,

$$F_1 = \tanh(\Phi_1^4) \quad F_2 = \tanh(\Phi_2^2) \quad (9)$$

The cross diffusion term  $D_\omega$ , defined in equation 10, blends the standard k-epsilon model and the standard k-omega model.

$$D_\omega = 2(1 - F_1)\rho\sigma - \omega, 2 \frac{1}{\omega} \frac{\partial k}{\partial x_j} \frac{\partial \omega}{\partial x_j}$$

(10)

The constants specific to the SST k-omega model are defined as:  $\sigma_{\omega,1} = 2.0$ ,  $\sigma_{\omega,2} = 1.168$ ,  $\sigma_{k,1} = 1.176$ ,  $\sigma_{k,2} = 1.0$ ,  $\alpha_1 = 0.31$ .

### 3. Numerical calculation method

This section presents a numerical calculation method for the hydrodynamic performance prediction of the planing boat. An implicit unsteady solver with SST k-omega turbulence model was used to solve the unsteady Reynolds Averaged Navier Stokes (uRANS) equations. The Volume of Fluid (VOF) approach was adopted in order to track the free surface boundary. The Dynamic Fluid Body Interaction (DFBI) was used to model the pitch and heave motions. The DFBI model allows the RANS solver to evaluate the force and moments on the hull and to solve the governing equations of body motion in order to relocate the body. CFD code STAR-CCM+ was used for grid generation and computations.

#### 3.1 Prismatic planing boat model, computational domain and boundary condition

Daniel Savitsky (1951, 1964) published a series of flat plates and prismatic planing boat models tests that gave rise to the first practical method of determining; the lift, resistance and the dynamic equilibrium of planing hulls. Since then, these models and methods have become widely applied in the field. For comparison purposes, this paper also selected one of the prismatic planing boat models. The model length (L) was 0.762m, width (B) was 0.127m, depth (D) was 0.152m, and the boat's slope angle was 20°. The model was generated and the experimental data obtained from literature. The three views of the model are shown in Fig. 1.

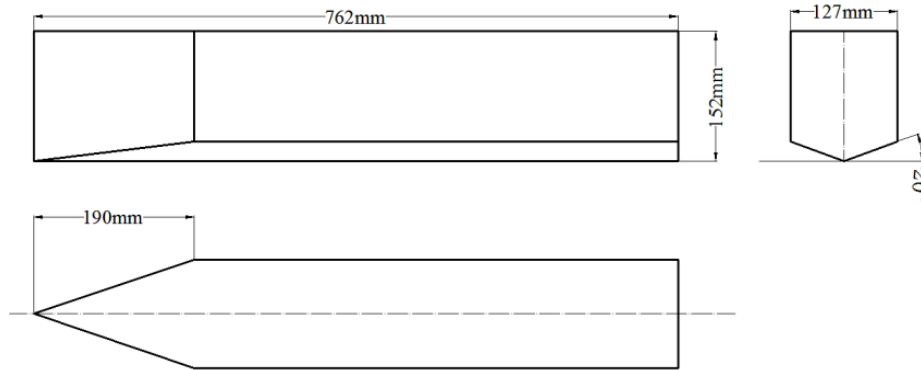
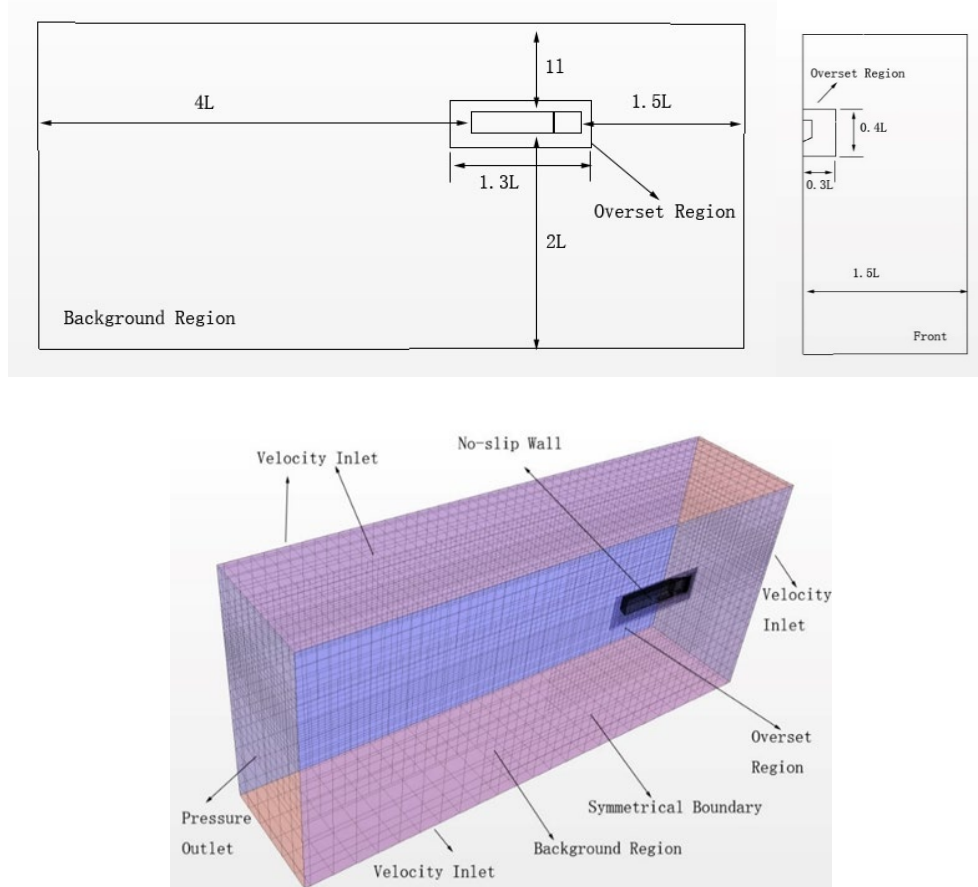


Fig. 1. Prismatic planing boat model

According to, Agostino De Marco et al. (2017) suggested that the boundaries should be placed far enough from the ship hull in order to avoid the well-known problem of wave reflection. In addition to these recommendations, the dimensions of the background region were chosen to ensure compliance with the ITTC's CFD recommendations (2011). It is important to note that in the ship's hydrodynamics field, no defined recommendations in terms of domain dimensions are available for the overset region.

The numerical calculation boundary conditions were set as follows. The surface of the boat was set as the no-slip wall boundary. The two faces were perpendicular to the direction of navigation: the one on the bow direction was set to the velocity inlet, and the other one on the stern direction was the

pressure outlet. Due to symmetry of the hull, the flow around the ship hull was assumed symmetrical with respect to the center plane. This is a typical boundary condition used in the CFD resistance test simulations, as indicated in the ITTC guide lines (2011). The effects of this assumption are negligible in terms of simulation results, as indicated in many works. This is also a reasonable assumption that leads to significant reduction in terms of computational time.



**Fig. 2.** The dimensions of the computational domain and the boundary conditions.

The numerical calculation boundary conditions were set as follows. The boat surface was set as the no-slip wall boundary. A velocity inlet condition was set on the upstream, bottom, top and side faces. A pressure outlet condition was set on the downstream plane. A symmetry plane condition was imposed on the longitudinal surface through the boat centerline.

Unsteady RANS simulations were performed on model speeds of 6.096m/s with the volume Froude numbers  $Fr \nabla = 4.54$ . The model was in a planing state, with a 6-degree trim angle, a length of soaked keel of 0.4686 m, a wetting length of 0.3302 m at the angle line, and the resistance of test value was 7.495 N.

### 3.2 Overset grid setup

Overset grid is useful when dealing with moving bodies involving fluid-structure interaction. With this grid implementation, mesh modification or deformation is not necessary providing great flexibility over the standard meshing techniques. Conservation of cell quality, which is typically considered at each time step is not an issue in overset grids. This also overcomes one of the drawbacks of deforming grids, when there are large body motions. In overset grid problems, a minimum of two regions is required: the background region enclosing the entire computational domain and a smaller region (overset) which contains the moving body. An overset interface is applied between the

background region and the overset region. At the interface, cells are grouped into active and inactive cells. Transport equations are only solved for active cells while inactive cells are not considered. Acceptor cells separating active and passive cells in the background region lie between the two regions which is used to couple solutions on the two over-lapping grids. Information passes from the active cells of one mesh to the active cells of the other through the acceptor cells. Acceptor cells accept values from the other region via interpolation of donor cell values (STAR-CCM+ User Guide). In order to ensure the accuracy of interpolation, the grid size should be kept in the same in the grid overlap area of the background region and the overset region. Overset meshing allows a planing boat to move freely throughout the computational domain without being artificially constrained by the mesh.

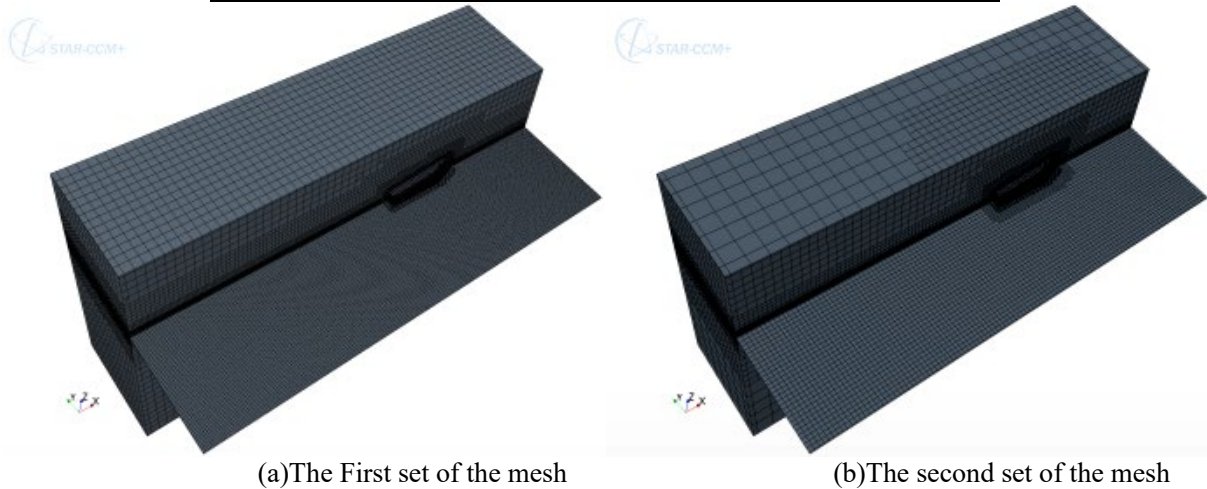
In this paper, the right-angle cutting grid was used to divide the computational domain grid. The right-angle grid cutting is able to adapt to the complex surface shape of the planing boat and obtain high computational efficiency and accuracy. On the surface of the boat, a body-fitting boundary layer mesh was used.

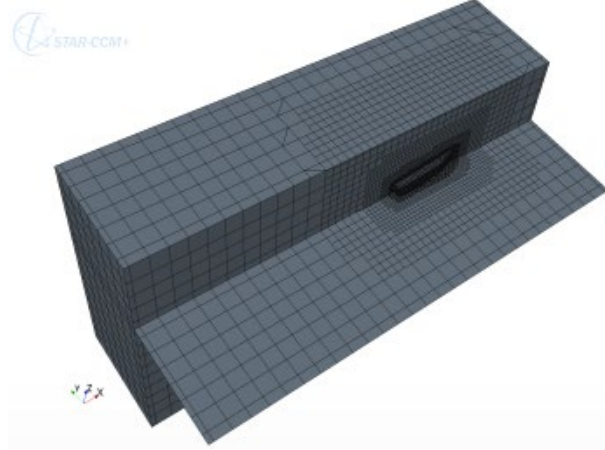
In order to determine the computational domain meshing scheme which was acceptable for both computational accuracy and computational efficiency, the present work used three sets of grids to examine different meshing schemes. It should be noted that, the refinement of the grids mainly focuses on the free liquid surface of the planing boat, the planing boat surface grid and the boundary surface of the calculation domain. In order to ensure that the VOF accurately captures the free surface, the mesh was refined with the aid of volumetric controls together with anisotropic refinement scheme. This scheme ensured that the mesh refinement size in Z direction is much smaller than that in X and Y directions. Uniform grid refinement ratio  $r_G = \sqrt{2}$  was chosen. The grid was systematically coarsened from fine to medium to coarse as illustrated in Fig. 3. Table 1 presents the summary of the obtained grids.

**Table 1.**

Number of cells for three grids

Grid scheme	The First set (refined)	The Second set (refined)	The Third set (coarse)
Number of grids (Ten thousand)	68.5	58.3	5.8





(c)The third set of the mesh

**Fig. 3.** Mesh of computing domain

### 3.3 Uncertainty analysis of numerical methods

The comparison between the calculated resistance values and the experimental values was shown in Table 2.

**Table 2.**

Comparison of calculated results of resistance using different meshing strategies

Grid scheme	1	2	3
Calculated resistance(N)	7.979	8.201	8.698
Tested resistance(N)	7.495	7.495	7.495
Deviation (%)	6.457	9.419	16.051

The above three grids correspond to fine encryption grid, medium encryption grid and coarse grid respectively. Taking the resistance results of three kinds of grid as an example, the uncertainty of setting of grid is analyzed. The numerical solutions of three kinds of meshes correspond to  $S_1$ ,  $S_2$ ,  $S_3$  respectively.

The numerical solution difference between the three grids is:

$$\varepsilon_{21} = S_2 - S_1 = 0.22N, \varepsilon_{32} = S_3 - S_2 = 0.497N \quad (11)$$

The convergence of the three set of grids is judged by the convergence factor  $R_G$ :

$$R_G = \frac{\varepsilon_{21}}{\varepsilon_{32}} = 0.442 \quad (12)$$

$0 < R_G < 1$ , the numerical solution exhibits monotonic convergence (Stern et al. 2016).

For the numerical solutions with monotonic convergence, the Richard extrapolation method can be used to estimate the errors caused by different grid settings.

$$U_G = F_G \delta_{REG}^* \quad (13)$$

$F_G$  is the safety factor,  $\delta_{REG}^*$  is the error estimate.

The degree of accuracy  $P_G$  is the obtained using equation 14.

$$P_G = \frac{\ln(\frac{\mathcal{E}_{32}}{\mathcal{E}_{21}})}{\ln r_G} = 2.35 \quad (14)$$

Error estimates due to differences between grid setup and encryption  $\delta_{RE_G}^*$  is:

$$\delta_{RE_G}^* = \frac{\mathcal{E}_{21}}{r_G^{P_G} - 1} = 0.175N = 2.33\%D \quad (15)$$

The error  $U_G$  is estimated based on Richard's extrapolation method, and the correction coefficient  $C_G$  is used instead of the safety factor. The correction coefficient  $C_G$  is given as:

$$C_G = \frac{r_G^{P_G} - 1}{r_G^{P_{G_{ext}}} - 1} = 2.153 \quad (16)$$

$|1 - C_G| > 0.125$ , and  $U_G$  is

$$U_G = [2|1 - C_G| + 1] \times |\delta_{RE_G}^*| = 0.539N = 7.72\%D \quad (17)$$

Relative error  $E = D - S_1 = 6.45\%D$

The uncertainty of the error  $U_V$  is:

$$U_V = \sqrt{U_{SN}^2 + U_G^2} = \sqrt{(0.0772)^2 + (0.042)^2} D = 7.91\%D \quad (18)$$

$|E| < U_V$ , the results of uncertainty show that the total error between experimental results and numerical results is less than the uncertainty.

In grid 1-3, due to grid encryption of necessary encryption areas, the three considered grids, normal convergence of numerical results was obtained, although there are differences in the accuracy of numerical results. The comparison of the solution for the fine grid against experimental results is 6.457%. According to ITTC guidelines, numerical prediction error of high-performance ships including planing boats should be controlled within 10%, hence grid 1 generation scheme grants adequate accuracy of numerical simulation. Continue to increase the degree of fine grid refinement is can continue to improve the precision of the simulation, but slightly increased with the increase of grid number to endless calculation precision on the engineering application and meaningless, after contrast and uncertainty analysis, the grid 1 encryption scheme have been able to meet the demand of the numerical prediction of normal, continue to encrypt the grid will only reduce the calculation efficiency.

#### 4. Resistance reduction hydrofoil design and performance calculation

##### 4.1 Hydrodynamic test of bare planing boat model

The above calculation method was based on a simple conventional planing boat model. Whether this method was suitable for the calculation of the hydrodynamic performance of a real planing boat with a complex shape still needed further verification. For this reason, this paper took the test model of a real planing boat (named USV01) as the research object, and verified the numerical calculation method based on the experimental data (Hailong Shen et al.2011).

The dimensions of the test model were as follows: length (Abbreviated as L) 2.75 meters, width (Abbreviated as B) 0.78 meters, height (Abbreviated as h) 0.325 meters, design draught (Abbreviated as d) 0.132 meters, displacement (Abbreviated as  $\Delta$ ) 125.4 kg, moment of inertia (Abbreviated as J)

58.6 kg·m<sup>2</sup>. The USV01 test model parameters were shown in Table 3. The section lines and 3D model of real boat were shown in Fig. 4 (a) and (b).

**Table 3.**

Test model parameters of USV01

Main feature	Symbol	Value	Unit
Scale ratio	k	1:4	
Overall length	L	2.75	m
Beam	B	0.78	m
Displacement	$\Delta$	125.4	kg
Draft	d	0.1325	m
Rotational inertia	J	58.6	kg·m <sup>2</sup>
Deadrise angle	$\beta$	18	deg
Longitudinal position of the center of gravity	$X_g$	1.048	m
Initial trim angle	$\tau$	0	deg

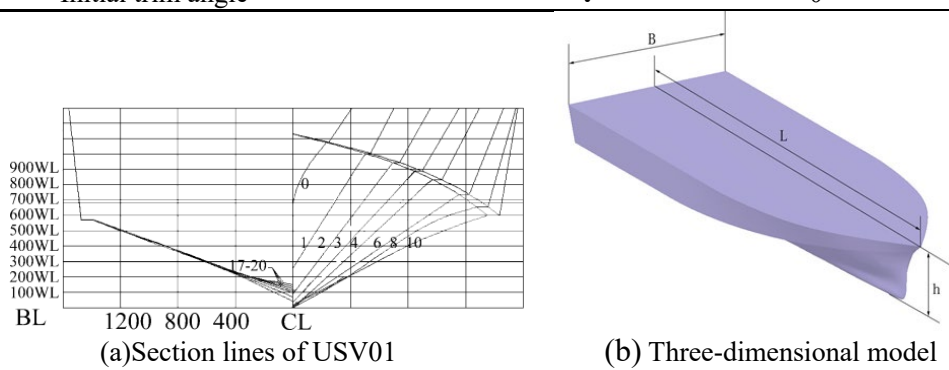
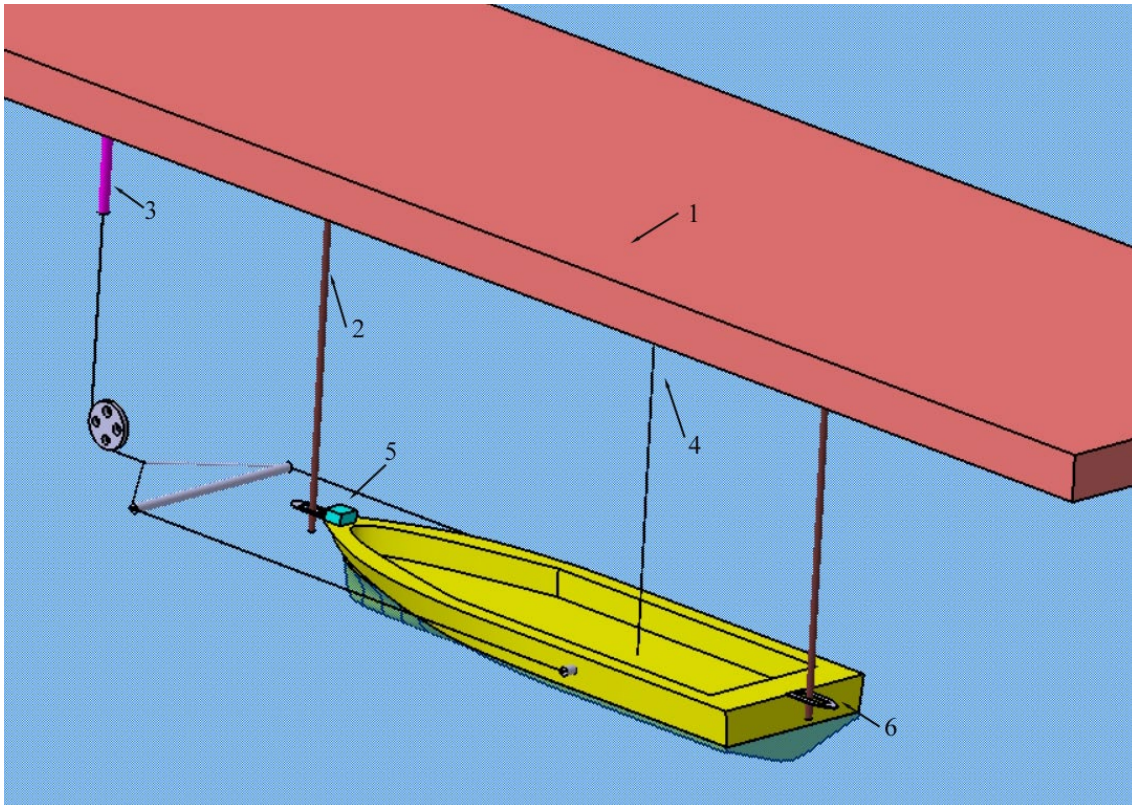


**Fig. 4.** Model of USV01

The experimental setup for the still water resistance test of USV01 is presented in Fig. 5. A pair of navigation rods is set at the front and rear ends of the hull model. The main function of rods is to restrict the lateral movement of the USV01 test model. The rods are set such that they do not affect the forward, dynamic sinkage, and trim movements. The towing point is located on the wide side and aligned with the USV01 test model center of gravity. The towing line is connected to the dynamometer via a fixed pulley. Please note that the dynamometer is connected to the carriage platform so that it can record the resistance of the hull during navigation. In order to measure the navigation attitude of the USV01 test model, the position sensor and gyroscope are installed at the center of gravity of the hull, which can accurately measure the trim and sinkage of the hull. Two high-speed cameras arranged before and after the model are used to record the flow of water around the hull.

The model tests were conducted in still water condition, in accordance to ITTC recommended procedures and guidelines. The minimum time between two consecutive towing processes was set at 10 minutes to ensure that the water level of the tank remains calm every time. It should be noted that the zero level of the sensor was initialized before each operation.



1. Carriage platform 2. Guide rod 3. Dynamometer  
4. Cable-extension displacement sensor 5. Gyroscope sensors 6. Guide plate

**Fig. 5.** Experimental setup

The towing speeds ranging from 1m/s to 15m/s were selected in the tests, including the design speed and maximum speed of vessel. The towing speed is from 1m / s to 15m / s, and 18 speed points are taken, and the Froude number ranges from 0.45 to 6.78. The experimental data are mainly used to verify the accuracy of the numerical method. The comparative analysis of experimental and numerical results is presented in Section 4.5

## 4.2 Hydrofoil design

### 4.2.1 Hydrofoil profile and design parameter definition

The most direct and effective way to reduce resistance is by changing the attitude of the craft to reduce the wetted surface area of the vessel when sailing at high speed. However, the position of the center of gravity of the gliding boat is hard to change after it is determined. In this paper, a fixed hydrofoil is installed at the bottom of the hull. To achieve the purpose of resistance reduction, the fixed hydrofoil can provide additional trim moment. This leads to a reduced wetted surface area without changing the position of center of gravity.

In this section, the USV01 model was used to research the effect of fixed hydrofoil on resistance. The design speed of the USV01 was set at 8 m/s which was the design speed. For comparative analysis, when the hydrofoil was installed, the weight and center of gravity of the USV01 model was kept constant. The designed hydrofoils consist the main hydrofoil and the support plate. NACA0012 profile was adopted for both the hydrofoil and support plate. The support plate chord length was 0.083m. The spacing between the two support plates was defined as  $b'$ , which was 0.1m. The fixed hydrofoil consisted of two trapezoidal hydrofoil splicing at the root of the hydrofoil. Hydrofoil parameters were defined as follows: The chord length of the hydrofoil tip was defined as  $l'$ , which was 0.092m. The chord length of the root was defined as  $l$ , which was 0.138m. The total span length was defined as  $b$ . Four (4) total span lengths were then investigated; 0.2B, 0.4B, 0.5B, and 0.6B, where B was the total width of the planing boat model. The hydrofoil shape and its parameters were

as shown in Fig.6(a).

The fixed hydrofoil was installed along the central keel line of the planing boat model. There were three variable installation parameters here. For the sake of simplification, they were defined as follows: Hydrofoil in the longitudinal position of the hull was defined as  $c$ , which was the distance from the main hydrofoil geometric center to the stern board. The longitudinal fixed position had three values namely  $c_0$ ,  $c_1$  and  $c_2$ .  $c_0$  was 0.086 meters,  $c_1$  was  $1/2L$ , and  $c_2$  was  $7/8L$ , where  $L$  was the length of the planing boat model. The installation height of the main hydrofoil was defined as  $h'$ , which was from the boat keel line to the main hydrofoil geometric center. The installation height had four values, which were  $0.05d$ ,  $0.35d$ ,  $0.65d$ , and  $0.95d$ , respectively, where  $d$  was the design draught of the planing boat model. Main hydrofoil angles of attack were defined as  $\theta$ , which was the angle between the section chord line and the boat keel line. Main hydrofoil angles of attack were also defined as follows: When the chord line coincides with the keel line, the angle of attack was zero; the angle between the chord line and the keel line was changed by rotating the chord line around the line across the Quarter-chord positions of support plates. The angle obtained by counterclockwise rotation was positive, while the angle obtained by clockwise rotation was negative. There were five angles of attack, which were  $-2$ ,  $-1.75$ ,  $-1$ ,  $0$  and  $1$  deg. The installation position of the hydrofoil on the ship and related parameter definition were as shown in Fig. 6(b).

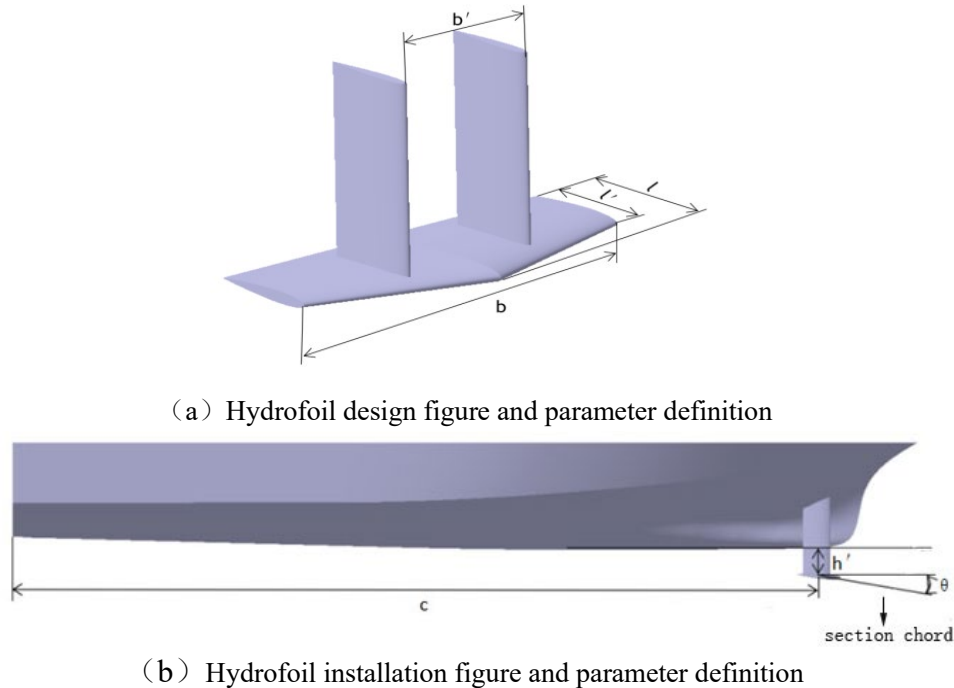


**Fig. 6.** Hydrofoil figure and parameter definition

#### 4.2.2 Hydrofoils with different parameters

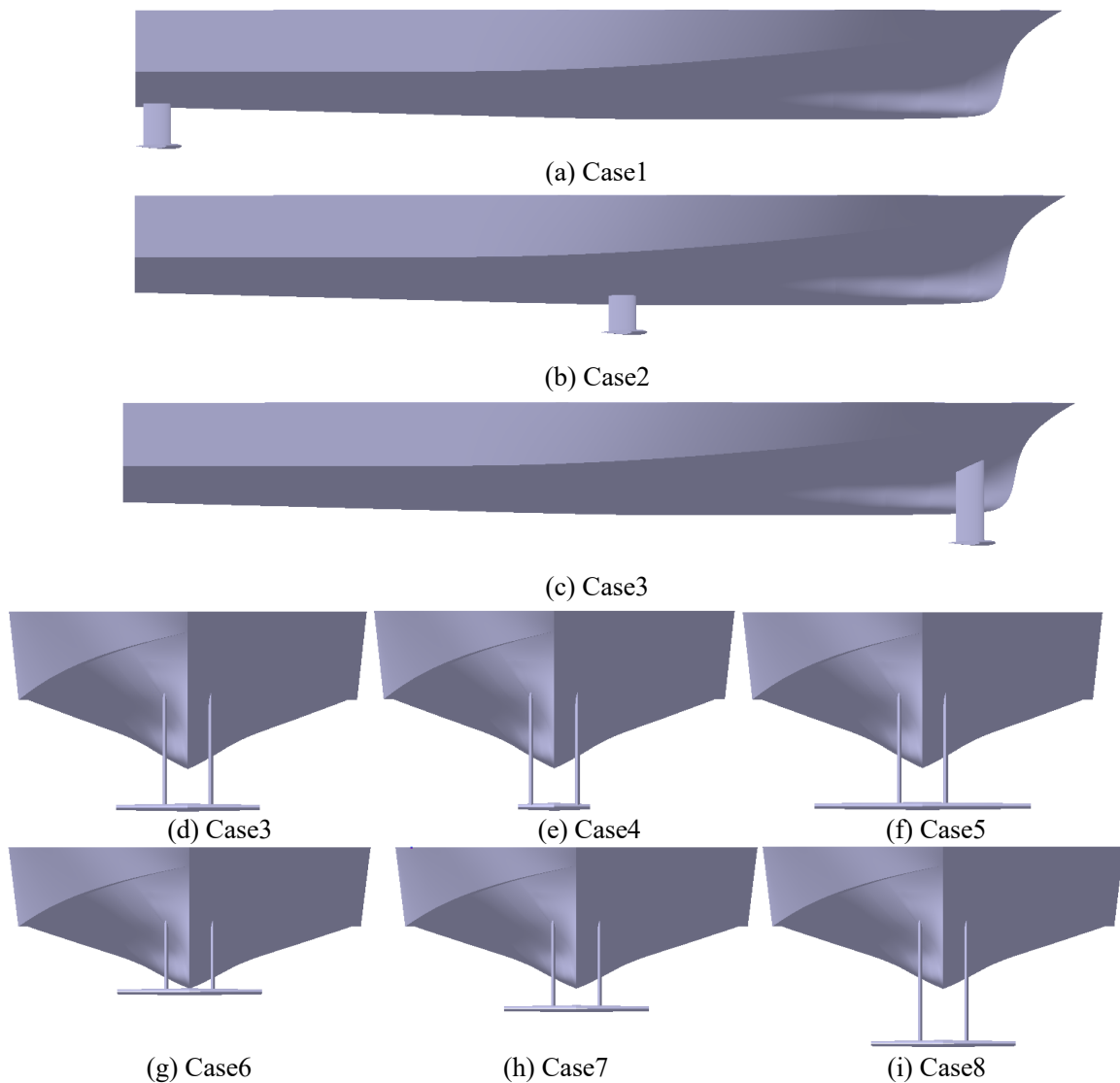
In order to study the resistance reduction effect of hydrofoil on the planing boat, four hydrofoil parameters were selected and combined to form twelve different hydrofoil cases. The four hydrofoil parameters were hydrofoil span, hydrofoil attack angle, hydrofoil installation height, and hydrofoil longitudinal position. The twelve different hydrofoil cases and the parameters combination are as shown in Table 4.

**Table 4.**  
Hydrofoil parameters and combination cases

cases	Hydrofoil design parameters				Hydrofoil installation parameters		
	$b/m$	$b'/m$	$l/m$	$l'/m$	$h'/m$	$\theta/$ degree	$c/m$
case1	0.312	0.1	0.138	0.092	0.086	0	0.086
case2	0.312	0.1	0.138	0.092	0.086	0	1.375

case3	0.312	0.1	0.138	0.092	0.086	0	2.406
case4	0.156	0.1	0.138	0.092	0.086	0	2.406
Case5	0.468	0.1	0.138	0.092	0.086	0	2.406
Case6	0.312	0.1	0.138	0.092	0.007	0	2.406
Case7	0.312	0.1	0.138	0.092	0.046	0	2.406
Case8	0.312	0.1	0.138	0.092	0.126	0	2.406
Case9	0.312	0.1	0.138	0.092	0.086	-2	2.406
case10	0.312	0.1	0.138	0.092	0.086	-1	2.406
case11	0.312	0.1	0.138	0.092	0.086	1	2.406
Case12	0.390	0.1	0.138	0.092	0.086	-1.75	2.406

The twelve hydrofoil cases are illustrated in Fig.7. Among them, case1, case2, and case3 mainly studied the influence of changes in the longitudinal installation position of the hydrofoil on the resistance of the planing boat. Case3, case4 and case5 were mainly to studied the influence of the variation of the hydrofoil span on the resistance of the planing boats. Case3, case6, case7 and case8 were mainly to compare the influence of the height change of the hydrofoil on the resistance of the planing boat. Case3, case9, case10, and case11 were mainly to compare the influence of the variation of the angle of attack of the hydrofoil on the resistance of the planing boat. Unlike other cases where only one parameter was changed at one time, case12 changed both the span and angle of attack. Case 12 was also taken as an example to study the resistance reduction effect of hydrofoil under different speeds of the planing boat.



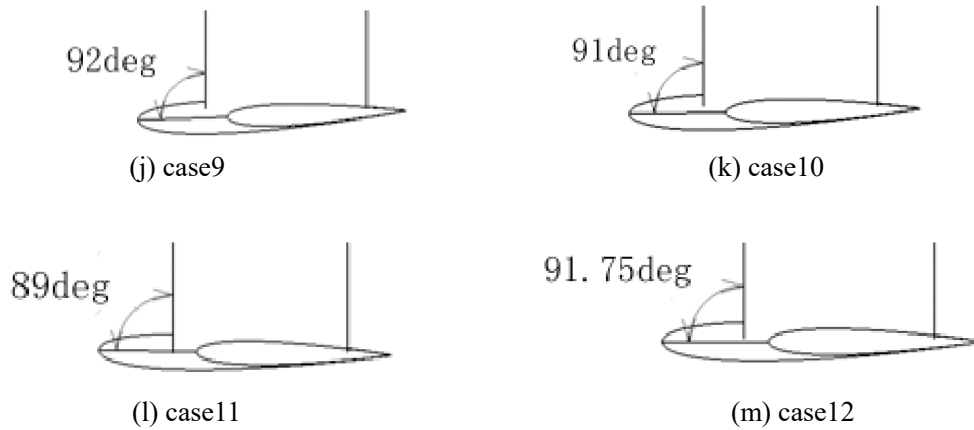


**Fig. 7.** Eleven types of hydrofoils

### 4.3 Computational Domains and Meshing

In this section, the size of the calculation domain was generated with reference to section 3, as illustrated in Fig.2. The grid was generated using the method recommended in section 3. The wall  $y^+$  value was taken as 250, and the height of the first layer mesh node on the hull was calculated according to formula (12). The size of the hull and hydrofoil surface grid were calculated using formulas (14) and (15). In order to reduce the computational deviation brought about by the different meshes, the bare hull and the hull with different hydrofoils cases adopted the same grid dimension and mesh generation strategy. Due to the similarity of grid generation in various cases, Fig. 9 demonstrates typical surface mesh of the hull and hydrofoil, the domain mesh and local grid.

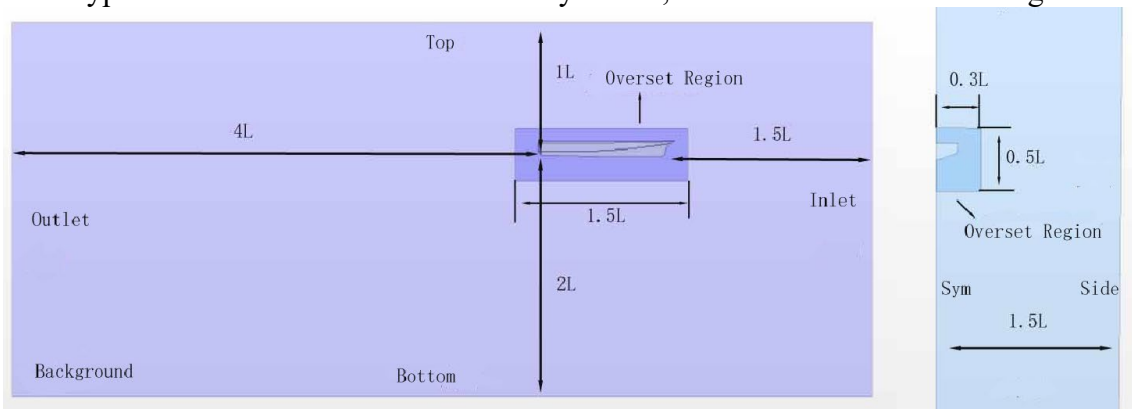
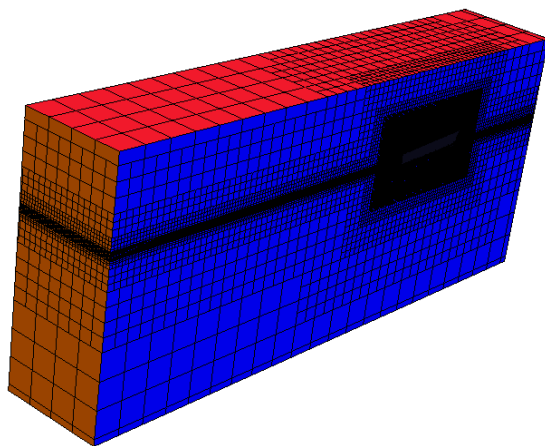
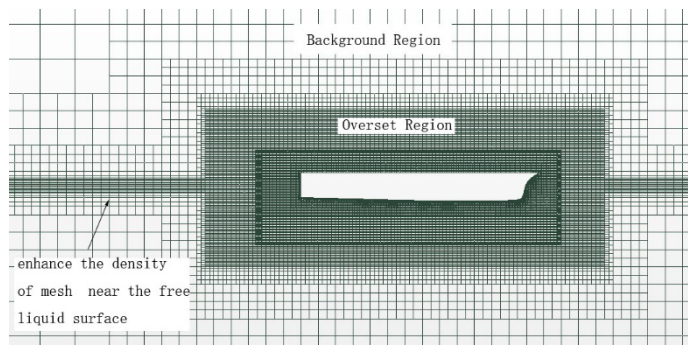


**Fig. 8.** The size of the calculation domain



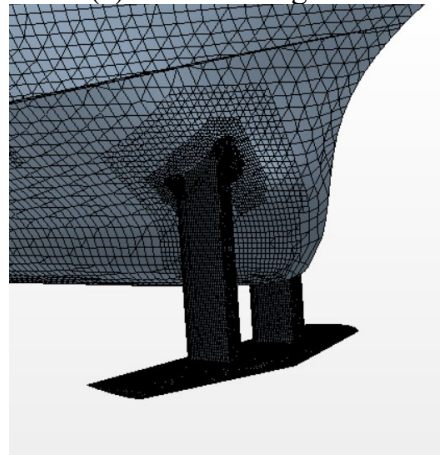
(a) Domain grids



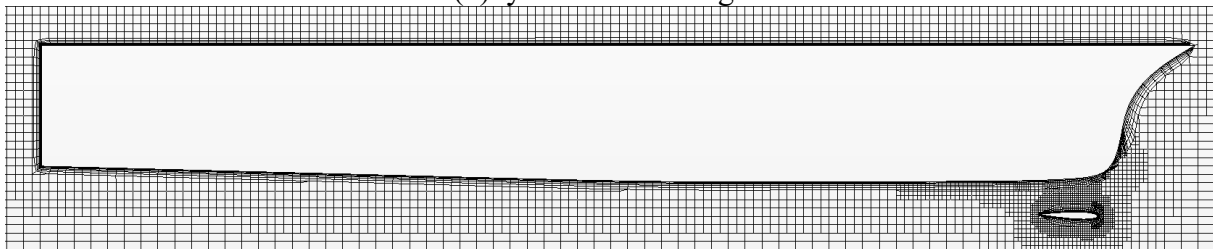
(b) Medium profile local grids



(c) hull surface grids



(d) hydrofoil surface grids



(e) Medium profile local grids

**Fig. 9.** Calculation grids

#### 4.4 Calculating operating conditions and boundary conditions

In this section, the calculation of the planing boat hydrodynamic performance was carried out using the method used in section 3.

##### 4.4.1 Bare planing boat model

With reference to the test speed value of the USV01 planing model, the following speeds were selected for numerical calculation: 2m/s, 4m/s, 6m/s, 8m/s, 10m/s, 12m/s, 15m/s. The boundary conditions were set. The hull surface was set as a non-slip wall boundary. The boundary of the overset region which was embedded in the background region was set as an overset mesh boundary. The boundary surface where the water flows out in the calculation domain was set as a pressure outlet. Only half of the hull symmetrical along the middle longitudinal section was retained in the calculation domain and the middle longitudinal section was set as the symmetrical boundary. Both the inflow boundary surface and the rest boundary surfaces were set as velocity inlet. The maximum physical time was set to 6s.

##### 4.4.2 Planing boat model with hydrofoils

In order to shorten the research period of the hydrofoil, under the premise of meeting the resistance reduction requirements of the design speed of the planing boat, the design speed (8m/s) of the planing boat was chosen to study the resistance reduction effect of the hydrofoil. In order to further study the resistance reduction effect of the hydrofoil at different speeds, and compare it with the resistance of

the bare planing boat, the following speeds were selected for case12: 2m/s, 4m/s, 6m/s, 8m/s, 10m/s, 12m/s and 15m/s. The corresponding real-boat speeds were 7.77kn, 15.55kn, 23.33kn, 31.10kn, 38.87kn, 46.65kn, and 58.32kn, respectively. In the setting of boundary conditions and calculation conditions, the only difference between the hull with hydrofoils and the USV01 model was that the hull with hydrofoils has no symmetry boundary conditions. This was due to the fact that the calculation models of hull with hydrofoils used the whole hull and hydrofoil, and the USV01 model used half of the hull calculation model based on the symmetry of the flow field and the hull. Furthermore, the other calculation conditions and settings for hull with hydrofoils and the USV01 model were exactly the same.

#### 4.5 Results and discussion

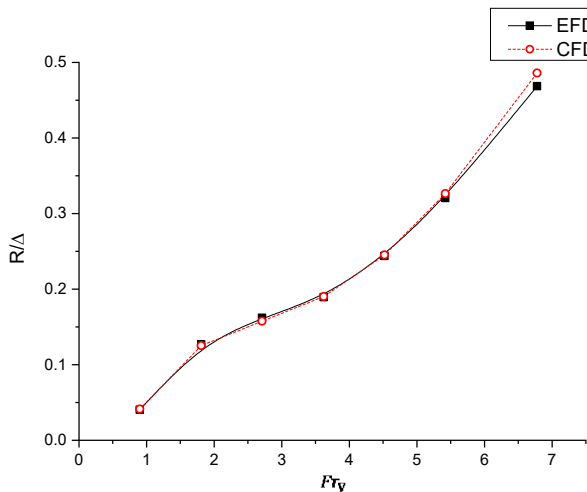
##### 4.5.1 USV01 calculation results

Table 5 showed the calculated values and experimental values of the resistance, sinkage, and trim angle of USV01 at various speeds. Compared with the test value, the calculated deviation of resistance was the largest at 15m/s, and the maximum deviation was 3.6%; the deviation of trim angle was the largest at 12m/s; the deviation of sinkage was greater after the speed exceeds 6m/s, but the general trend was consistent with the experimental value. The above calculation results show that the method for calculating the resistance of the planing boat adopted in this paper was suitable and has reliable calculation accuracy. Fig.10 showed the comparison of calculated and experimental values for resistance, sinkage and trim angle at different speeds. From the figure, it is seen from that the numerical results of the resistance and trim angle agree well with the experimental results.

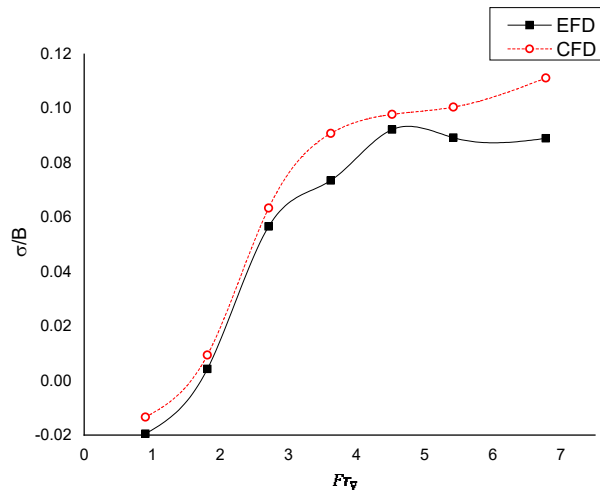
**Table 5.**

USV01 calculated and experimental values of Resistance, sinkage and trim angle at different speeds

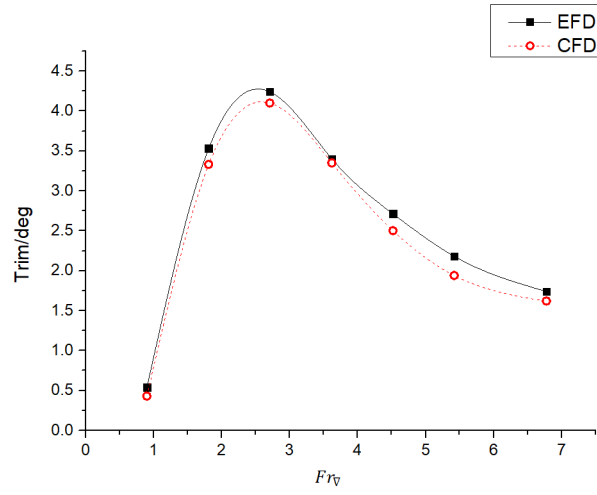
U(m/s)	$Fr_V$	Resistance(N)			Sinkage(mm)			Trim(deg)		
		EFD	CFD	Deviation	EFD	CFD	Deviation	EFD	CFD	Deviation
2	0.90	49.29	50.54	2.54%	-15.21	-10.42	-31.58%	0.54	0.43	-20.37%
4	1.81	154.94	152.72	-1.43%	3.35	7.32	121.21%	3.53	3.33	-5.67%
6	2.71	197.67	192.32	-2.71%	44.21	49.52	11.99%	4.24	4.1	-3.30%
8	3.62	231.08	232.07	0.43%	57.41	70.92	23.52%	3.4	3.35	-1.47%
10	4.52	297.33	299.27	0.65%	71.98	76.37	6.12%	2.71	2.5	-7.75%
12	5.42	391.12	398.33	1.84%	69.67	78.42	12.64%	2.18	1.94	-11.01%
15	6.78	571.54	593.08	3.77%	69.49	86.81	25.07%	1.74	1.62	-6.90%



(a) Resistance



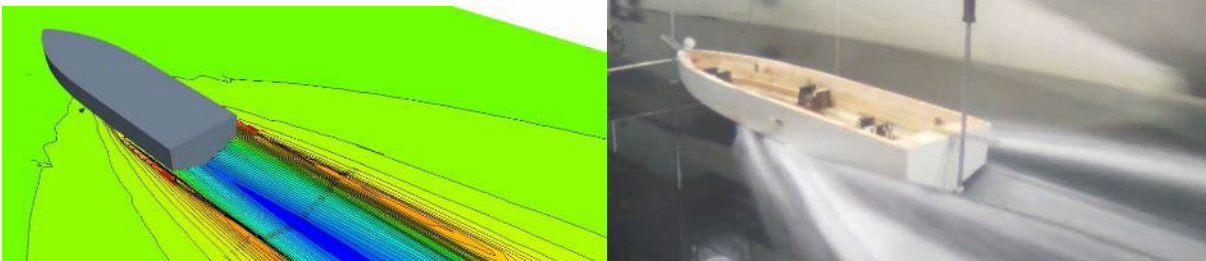
(b) Sinkage



(c) Trim

**Fig. 10.** Comparison of the calculated results with the test results( $\Delta=125.4\text{kg}$ ,  $X_g=1.048\text{m}$ )

This paper also successfully simulated the wake of the planing boat, but the simulated splash was not obvious, as shown in Fig.11. Further analysis showed that there was a clear difference between the wake obtained from the numerical simulation and the test wake at 15m/s, indicating that the numerical calculation method used in this paper needed further improvement in the simulation of droplets and wake.



(a) Simulated wake and splash

(b) Tested wake and splash

**Fig. 11.** Wake and splash of planing boat

#### 4.5.2 Resistance reduction effect of different hydrofoils at 8 m/s

##### 4.5.2.1 Effect of hydrofoil longitudinal position on resistance reduction

The calculated results of the resistance, trim angle and sinkage of the planing boats with the hydrofoils which had different longitudinal installation positions were shown in Table 6 and Fig. 12. From Table 6, the hydrofoils installed near the bow ( $c=7/8L$ ), stern ( $c=c_0$ ), and midship ( $c=1/2L$ ) had a significant effect on the resistance and sailing state of the boat. When the hydrofoil was installed at the stern, the total resistance increased significantly by 12.5% compared to the USV01. This was mainly due to the fact that the hydrodynamic lifting force lifted the stern and sank the bow, resulting in a reduction in the trim angle and the sinkage at the center of gravity compared to the USV01. When the hydrofoil was installed near the bow position, the total resistance decreased by 27.5%, and the resistance reduction effect of the hydrofoil was significant. This was mainly due to the fact that the hydrodynamic lifting force lifted the bow and sank the stern, which significantly increased trim and sinkage at the center of gravity. When the hydrofoil was installed in the middle of the hull, sinkage at the center of gravity increased and the trim became smaller than the USV01, leading to a rise in resistance by 6.9%.

**Table 6.**

Effect of hydrofoil longitudinal position on resistance reduction

Item	Longitudinal position (c)	Total resistance /N	Resistance reduction percentage /%	Sinkage/mm	Trim/deg
------	---------------------------	---------------------	------------------------------------	------------	----------

USV01	N	229.19	N	70.94	3.35
Case1	0	257.86	-12.5	65.32	2.82
Case2	1/2L	244.96	-6.9	73.85	3.05
Case3	7/8L	166.18	27.49	94.43	3.87

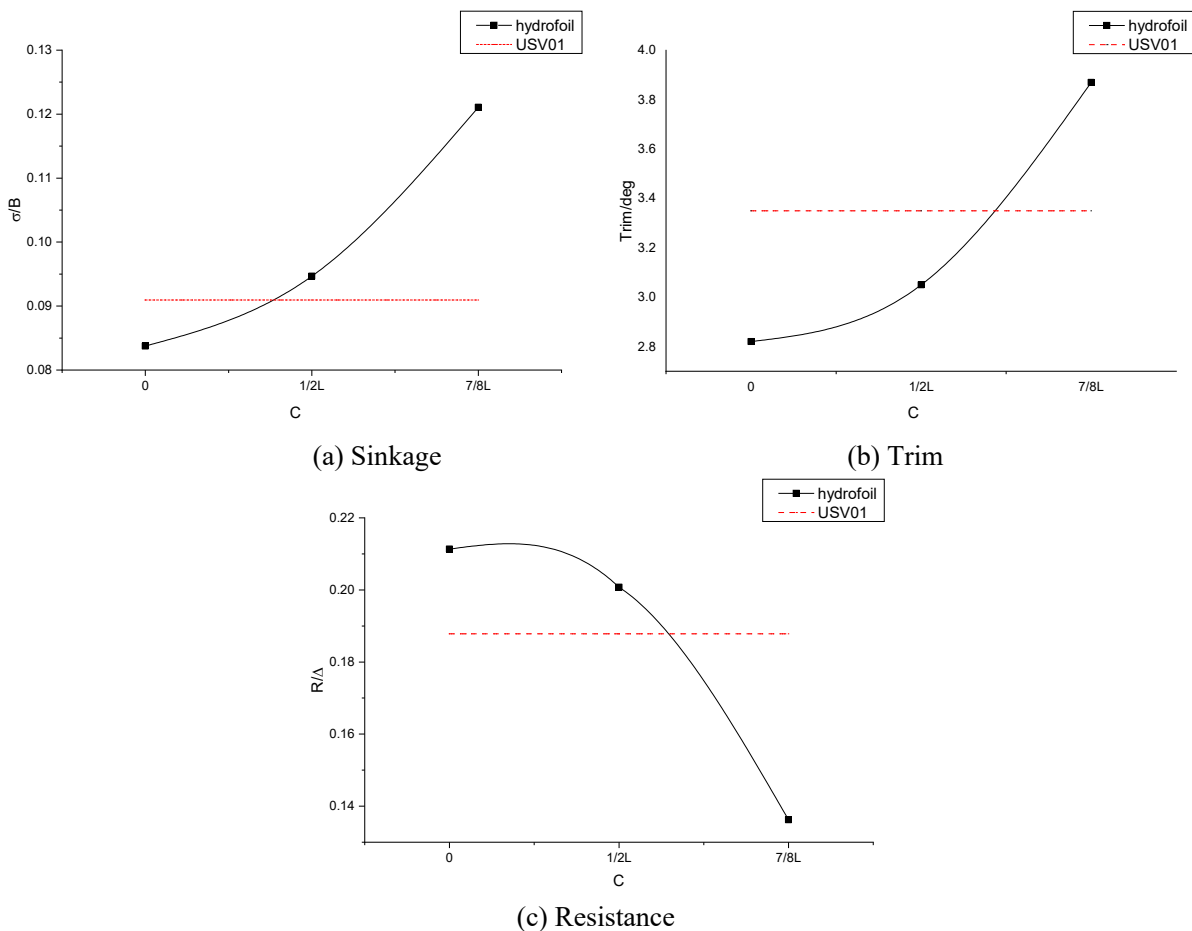
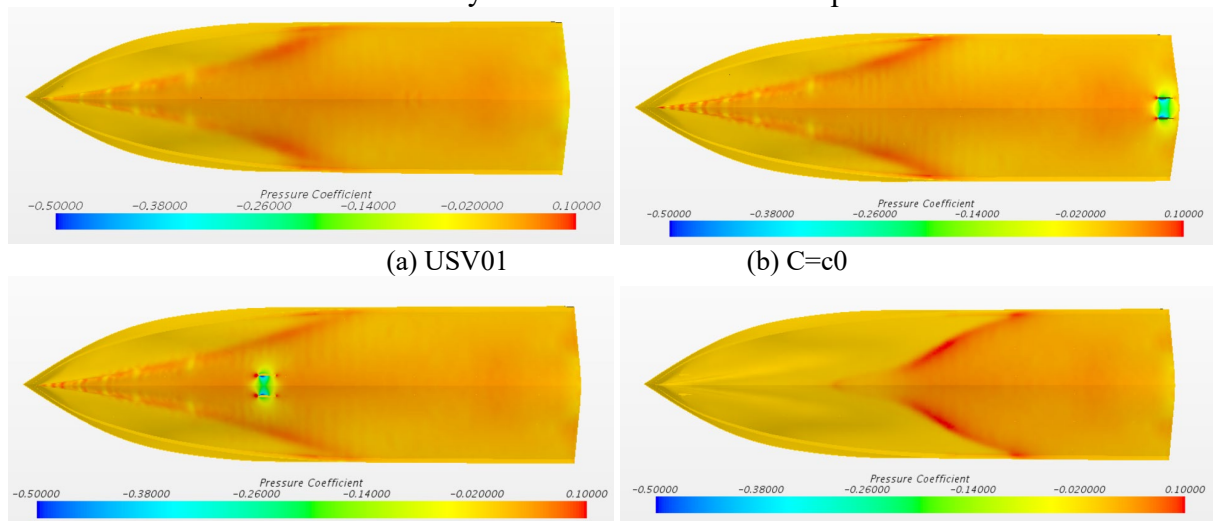


**Fig. 12.** Effect of hydrofoil longitudinal position on attitude and resistance

Fig.13 showed the distribution of dynamic pressure on the bottom of the boat. It was obvious that with the change of the installation position of the hydrofoil, the position of the maximum dynamic pressure at the bottom of the boat had also changed significantly. At  $c=7/8L$ , the change in dynamic pressure position was the most significant and very beneficial to increase the trim angle. The highest resistance reduction effect due to the hydrofoil was realized at this position.



(c)  $C=1/2L$ (d)  $C=7/8L$ **Fig. 13.** Effect of hydrofoil longitudinal position on dynamic pressure distribution of hull

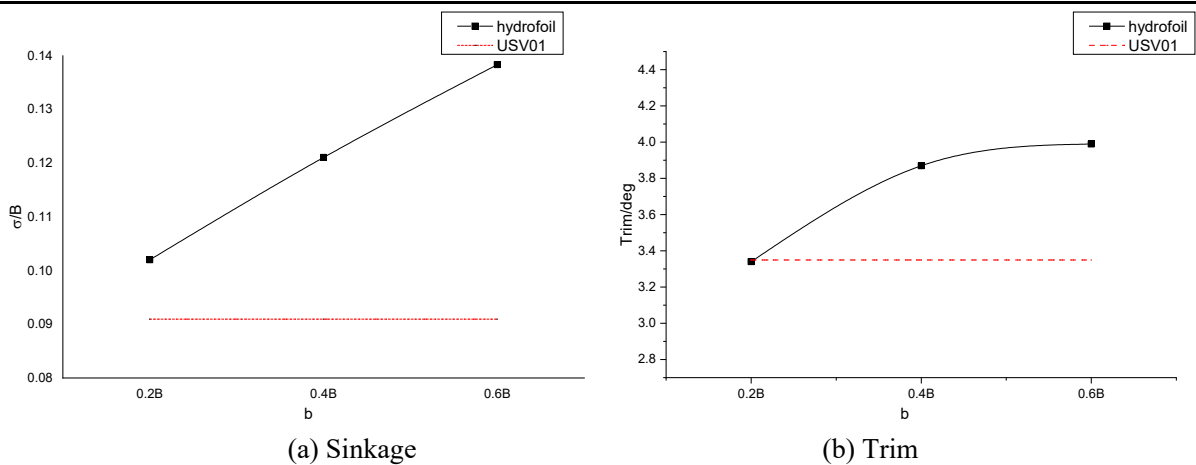
#### 4.5.2.2 Effect of hydrofoil span on resistance reduction

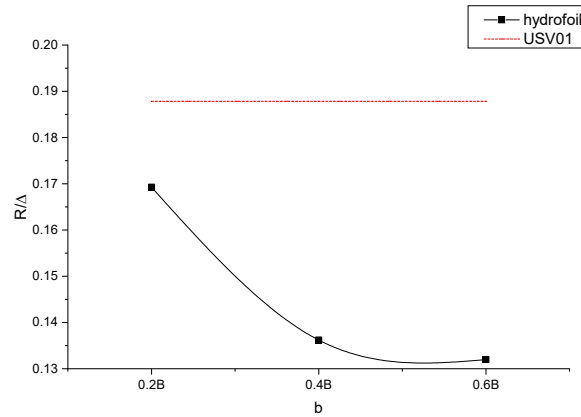
The calculated results of the resistance, trim angle and sinkage of the planing boats corresponding to the different hydrofoil spans were shown in Table 7 and Fig.14. Table 7 demonstrates that with the variation of the hydrofoil span, the resistance value and the sailing attitude of the planing boat were significantly changed compared with the USV01. The sinkage at the center of gravity and resistance reduction effect of the hydrofoil significantly increased with the increase of the span length. Resistance reduction was highest at  $b=0.6B$ , and the resistance reduction effect reached 29.74%. After installing the hydrofoil, the trim angle did not change much at  $b=0.2B$ , and it slightly increased at  $b=0.4B$ .

In order to gain insight on the influence of the hydrofoil span on the flow around the hull, pressure distribution is presented (*see Fig. 15*). The figure shows the distribution of dynamic pressure on the bottom of the hull with different hydrofoil span lengths. At  $b=0.2B$ , the dynamic pressure distribution at the bottom surface of the hull with hydrofoil was basically the same as that of the USV01, which is consistent with minimal changes in the trim angles presented in Table 7. At  $b=0.4B$  and  $0.6B$ , the position of the maximum dynamic pressure distribution significantly shifted backwards with the increase of the span length, which was favorable for increasing the trim angle of the planing boat. It is obvious that the increase in the span length represented an increase in the area of the hydrofoil. Therefore, an appropriate increase in the area of the hydrofoil can help to reduce the resistance of the planing boats by generating some forward lift.

**Table 7.**  
Effect of hydrofoil span on resistance reduction

Item	span length (b)	Total resistance /N	Resistance reduction percentage /%	Sinkage/mm	Trim/deg
USV01	N	229.19	N	70.94	3.35
Case4	0.2B	206.49	9.9	79.57	3.34
Case3	0.4B	166.18	27.49	94.43	3.87
Case5	0.6B	161.04	29.74	107.93	3.99





(c) Resistance

**Fig. 14.** Effect of hydrofoil span on attitude and resistance

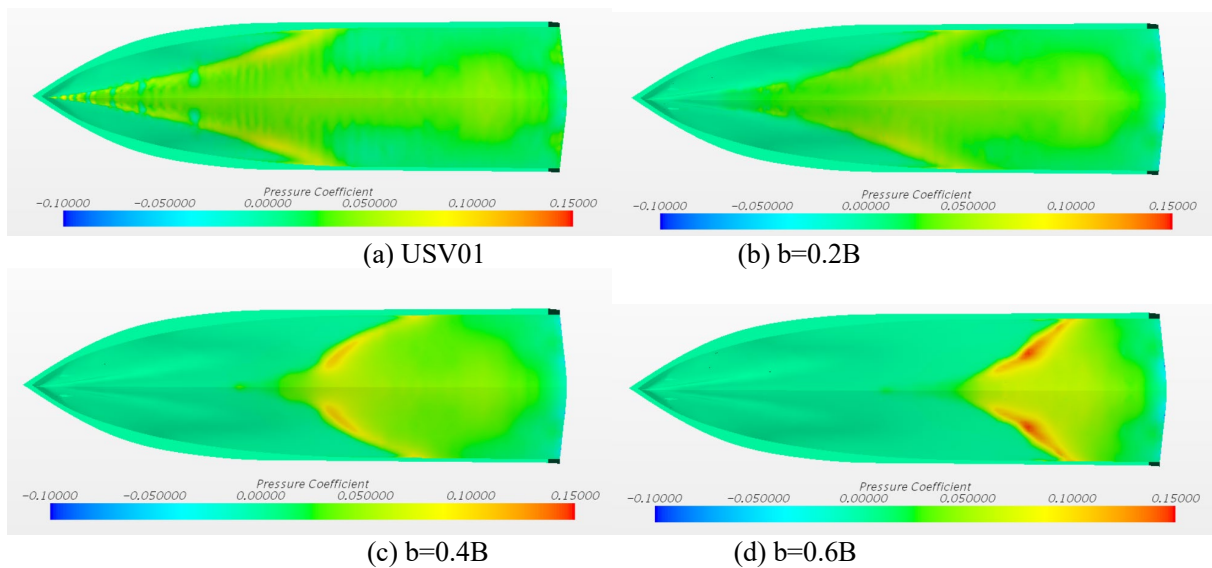


**Fig.15.** Effect of hydrofoil span on dynamic pressure distribution of hull

#### 4.5.2.3 Effect of hydrofoil installation heights on resistance reduction

The influence of the installation height of the hydrofoil on the resistance and sailing state of the planing boat is presented in Table 8 and Fig. 16. It is evident that after the installation of the hydrofoil, led to a significant drop in resistance. On the other hand, the trim angle and the sinkage both increased in different degrees. When the installation height increased from 0.05d to 0.35d, the percent reduction in resistance increased significantly by 11.68%. When the installation height increased from 0.35d to 0.65d, the percent reduction in resistance increased by only 4.61%. When the installation height increased from 0.65d to 0.95d, the percent reduction in resistance only increased by 3.25%. Obviously, when the installation height was greater than 0.35d, the resistance reduction gains obtained by increasing the height of the hydrofoil installation are expected become smaller and smaller.

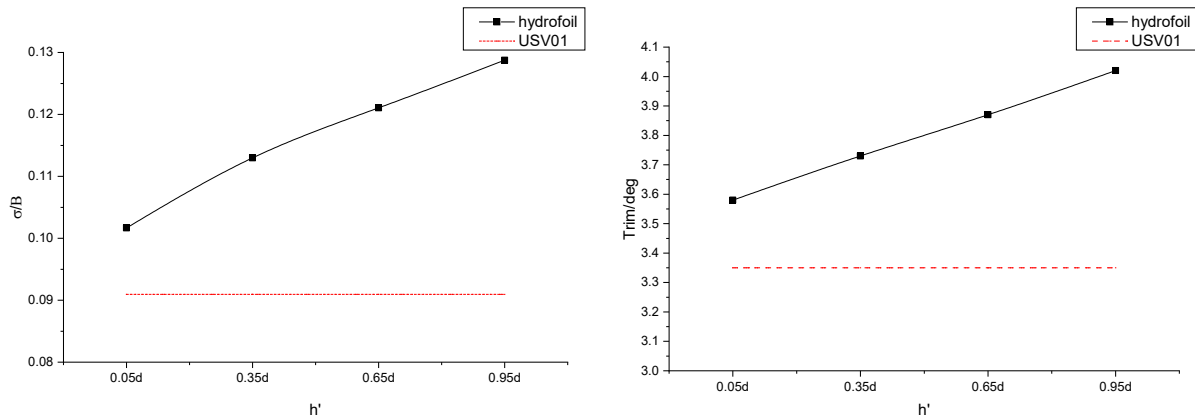
Fig. 17 showed the distribution of dynamic pressure on the hull when the boat was fitted with hydrofoil at different heights. It is clear that with the increase of the installation height of the hydrofoil, the maximum dynamic pressure distribution position on the hull continued to shift backwards, which was conducive to increasing the trim angle and improving the sailing state, thereby reducing the total resistance.

**Table 8.**

Effect of installation heights on resistance reduction

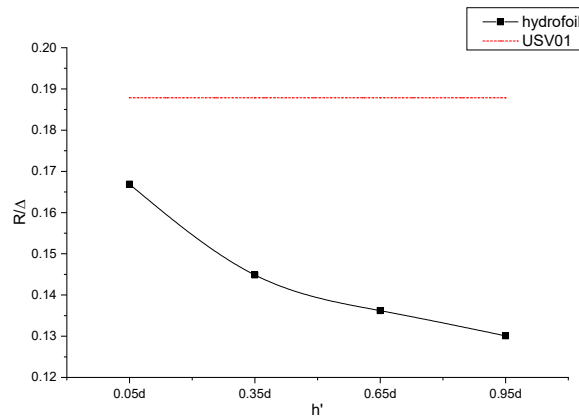
Item	Installation height( $h'$ )	Total resistance /N	Resistance reduction percentage /%	Sinkage/mm	Trim/deg
------	-----------------------------	---------------------	------------------------------------	------------	----------

USV01	N	229.19	N	70.94	3.35
Case6	0.05d	203.62	11.2	79.31	3.58
Case7	0.35d	176.75	22.88	88.12	3.73
Case3	0.65d	166.18	27.49	94.43	3.87
Case8	0.95d	158.73	30.74	100.43	4.02



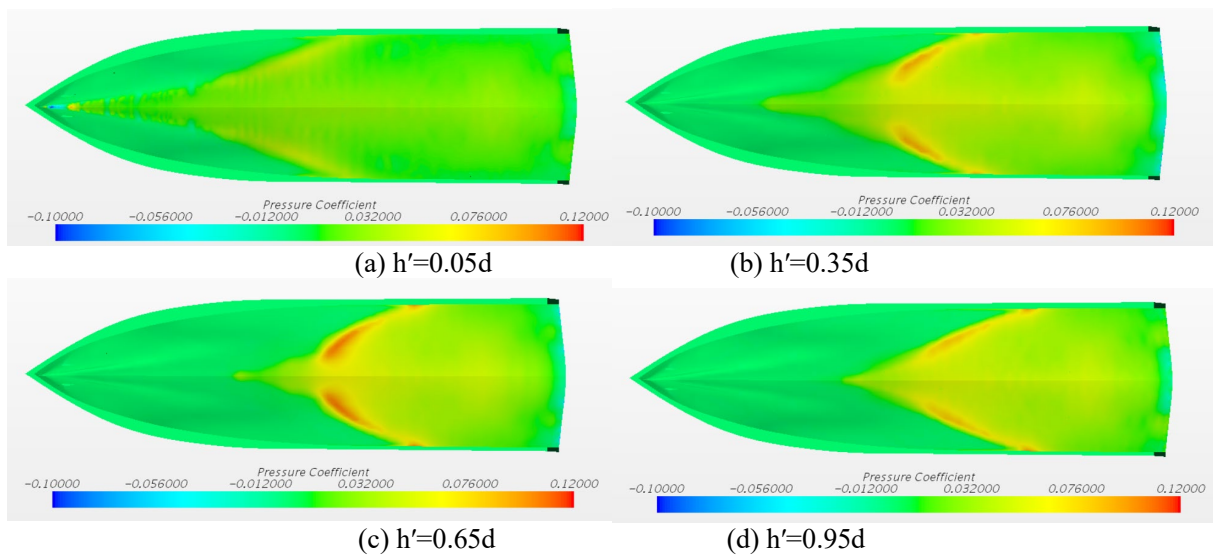
(a) Sinkage

(b) Trim



(c) Resistance

**Fig. 16.** Effect of installation heights on attitude and resistance



(a)  $h'=0.05d$

(b)  $h'=0.35d$

(c)  $h'=0.65d$

(d)  $h'=0.95d$

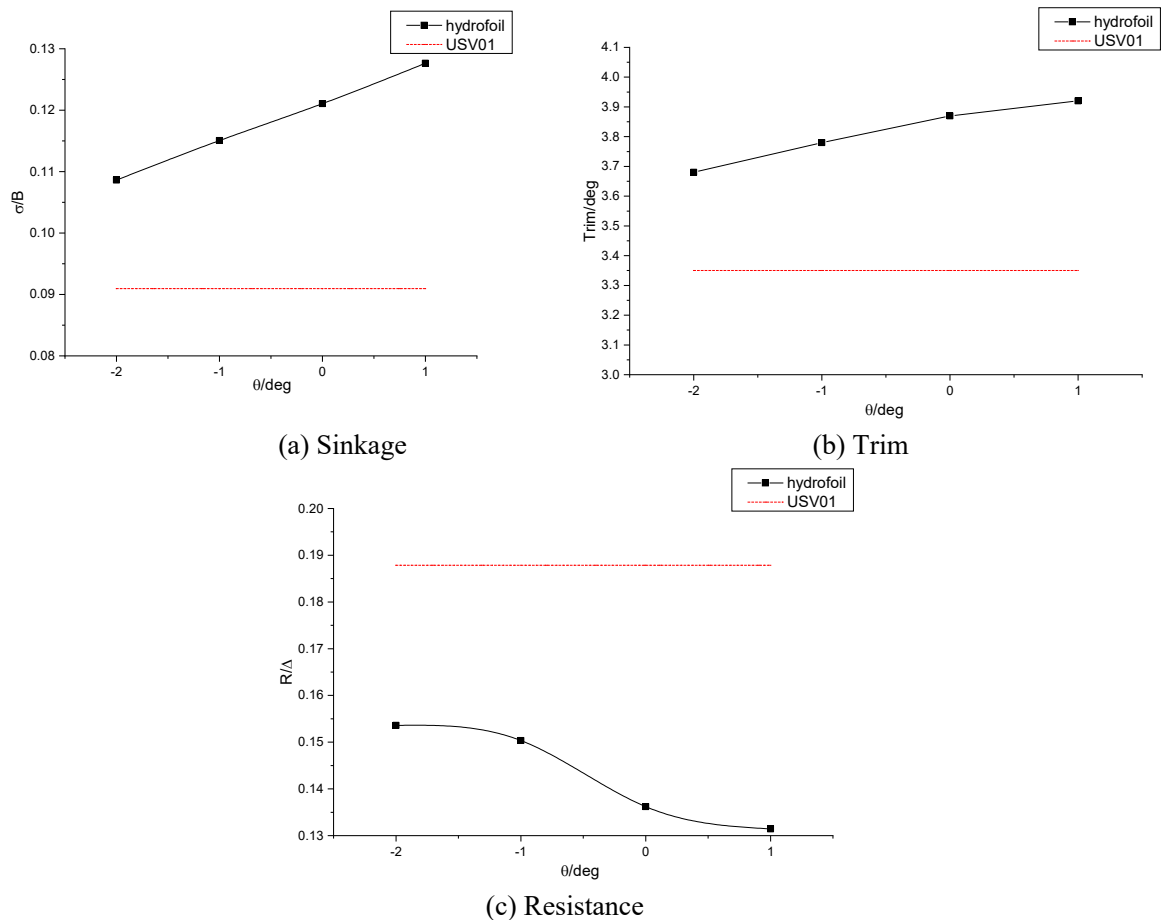
**Fig. 17.** Effect of hydrofoil installation heights on dynamic pressure distribution of hull

#### 4.5.2.4 Effect of hydrofoil attack angle on resistance reduction

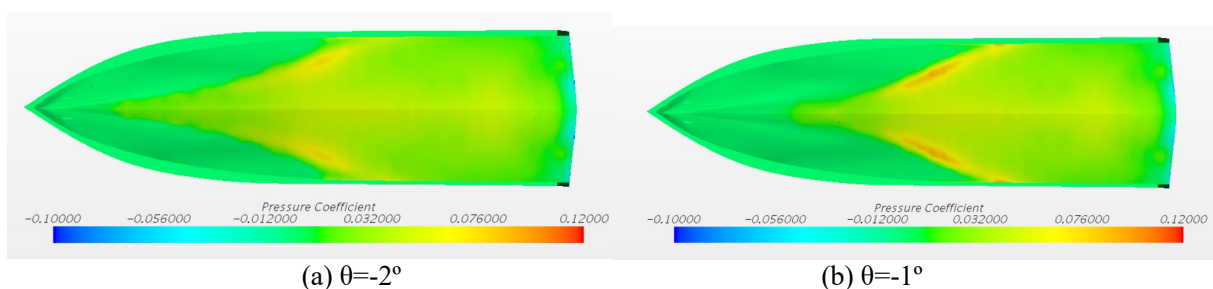
Table 9 and Fig. 18 presents the calculation results of the influence of the hydrofoil attack angle on the resistance and sailing state. In general, boat resistance of the planing boat decreased significantly, and the, trim angle and the sinkage both increased in different degrees. When the attack angle decreased from 0 degrees to -2 degrees, the percent reduction in resistance also gradually reduced. When the attack angle increased from 0 degree to 1 degree, the percent reduction in resistance increased by only 2.53%. Obviously, zero angle of attack and positive angle of attack were more suitable in reducing the resistance of the planing boat.

**Table 9.**  
Effect of hydrofoil attack angle on resistance reduction

Item	Hydrofoil attack Angle $\theta$ /deg	Total resistance /N	Resistance reduction percentage /%	Sinkage/mm	Trim/deg
USV01	N	229.19	N	70.94	3.35
Case9	-2	187.38	18.24	84.72	3.68
Case10	-1	183.45	19.95	89.74	3.78
Case3	0	166.18	27.49	94.43	3.87
Case11	1	160.39	30.02	99.56	3.92



**Fig. 18.** Effect of hydrofoil attack angle on attitude and resistance



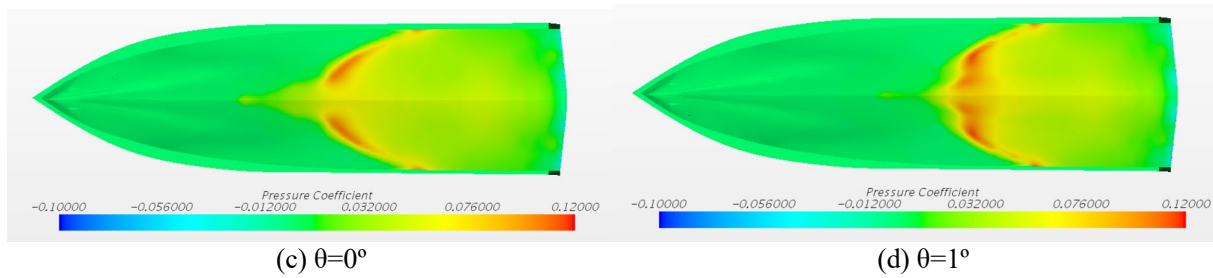


**Fig. 19.** Effect of hydrofoil attack angle on dynamic pressure distribution of hull

The dynamic pressure distribution on the hull at different foil angles of attack are presented in Fig. 19. With the increase of the attack angle of the hydrofoil, the maximum dynamic pressure distribution position on the surface of the bottom continued to shift backwards. This resulted to an increase in trim angle and improved sailing state, thereby reducing the total resistance. Although, a positive hydrofoil attack angle has a better resistance reduction effect, the high heave and trim values may lead to a concentrated stern load at high speeds. This is evident from Fig.19 (d), where the pressure concentration area is closer to the stern, compared with other cases. When the pressure concentration area of stern is too concentrated, the dolphin movement is likely to occur at high speed.

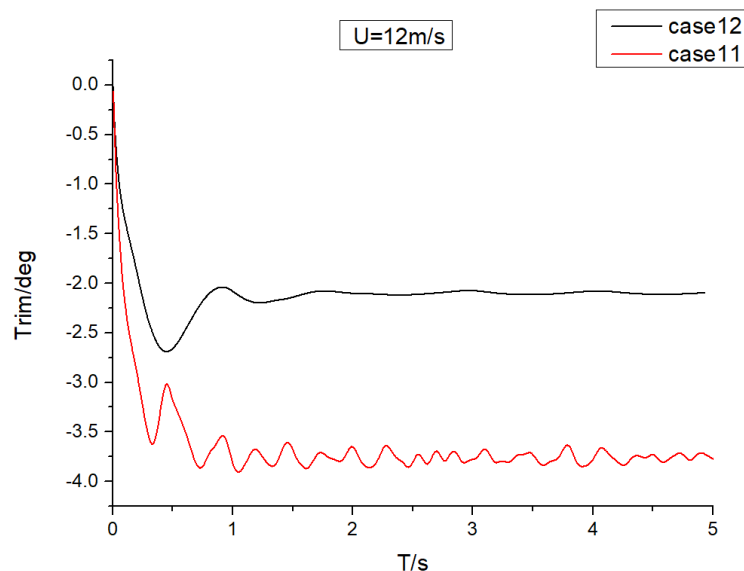


**Fig. 20.** Comparison of the trim curves of Case12 and Case11 at  $U=12\text{m/s}$

To further put this into context, a comparison of trim curves for Case11 and Case12 at  $U=12\text{m/s}$  is presented (see Fig. 20). It is observed that the trim curves for Case12 converges smoothly and tends to be stable, while the trim curves for Case11 appears to have irregular vibrations. Although the resistance reduction effect of positive hydrofoil attack angle is better at medium speed, a negative effect on stability is likely at high speed. This is in agreement with the findings by [Bi and Shen \(2019\)](#). In the study, they noted that in the regular waves, the positive hydrofoil angle of attack makes the draught of the hull to decrease greatly at high speed. Hence, the vessel has inadequate pitch damping, leading to a rapid increase in motion response amplitudes, which could worsen the boat seakeeping. In this regard, negative hydrofoil angle of attack angle should be selected.

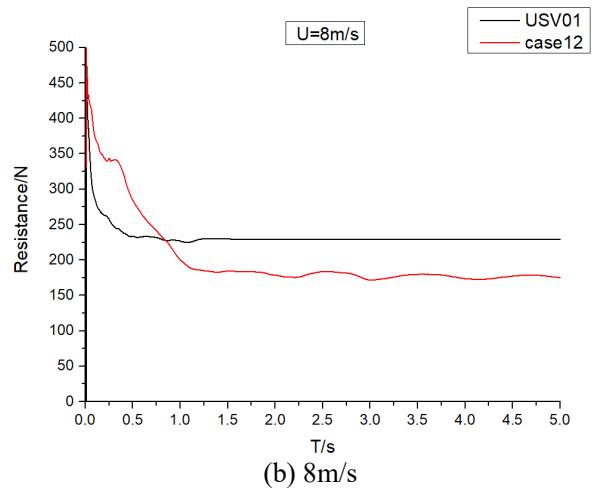
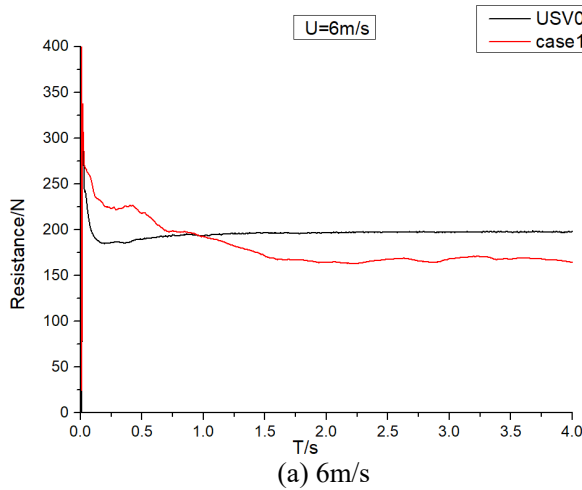
#### 4.5.3 Case 12 resistance reduction effect of hydrofoil at different speeds

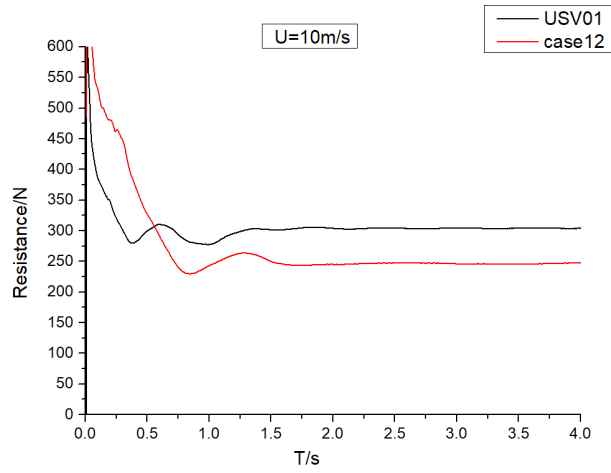
From the above results, it was clear that installed hydrofoil at  $7/8$  boat length can significantly reduce the resistance of the planing boats at  $8\text{m/s}$ . Case 12 was selected to further study the resistance reduction effect of hydrofoil at different speeds. Fig.21 showed the convergence of resistance for USV01 at  $6\text{m/s}$ ,  $8\text{m/s}$  and  $10\text{m/s}$ . The calculation results were shown in Table 10 and Fig.21. In order to facilitate comparison of the resistance reduction effect of the hydrofoil, Table 10 and Fig.22 also gave the calculation results of the resistance and sailing state of USV01.

Fig.22 showed that after installing the hydrofoil, case 12 had a significant increase in trim angle and sinkage at different speeds compared to USV01. Also note that the increase in trim angle at 6 m/s was the most significant. In addition, the resistance of case 12 with hydrofoils was larger than the conventional USV01 at low speeds (2m/s and 4m/s) and high speeds (12m/s and 15m/s). This meant that it is difficult to achieve a significant reduction in the resistance of the planing boat for all speeds by installing the hydrofoils in the proper position. However, by properly designing and installing hydrofoils, the resistance of a planing boat at a particular speed or within a range of speeds can be significantly reduced. Compared with the USV01, by installing the hydrofoil, the resistance can be reduced by 23.07% at 8m/s (corresponding to a speed of 31.1kn of a real ship) and 17.66% at 10m/s (corresponding to a speed of a real ship of 38.87kn). When the speed exceeds 12m/s(46.65knots), the hydrofoil may have added resistance which becomes significant at 15m/s(58.32 knots). The added resistance in this scenario forms 19.09% of the bare boat total resistance. The resistance reduction effect of hydrofoil is obvious at medium speeds, and the applicable speed of hydrofoil shall not exceed 12m/s.

**Table 10.**  
Resistance and sailing states at different speeds of USV01 and case12

U(m/s)	$Fr_{\nabla}$	Resistance(N)		Resistance reduction(%)	Sinkage(mm)		Trim(deg)	
		USV01	case12		USV01	case12	USV01	case12
2	0.90	50.54	54.82	-8.47	-10.42	-11.38	0.43	0.24
4	1.81	152.72	157.95	-3.42	7.37	16.12	3.33	3.62
6	2.71	192.32	169.31	11.96	49.52	68.78	4.10	4.68
8	3.62	229.19	176.32	23.07	70.97	86.72	3.35	3.57
10	4.52	299.27	246.41	17.66	76.32	92.67	2.50	2.81
12	5.42	398.33	408.98	-2.67	78.49	89.82	1.94	2.09
15	6.78	593.08	706.30	-19.09	86.88	85.33	1.62	1.57





(c) 10m/s

Fig. 21. Resistance convergence curve

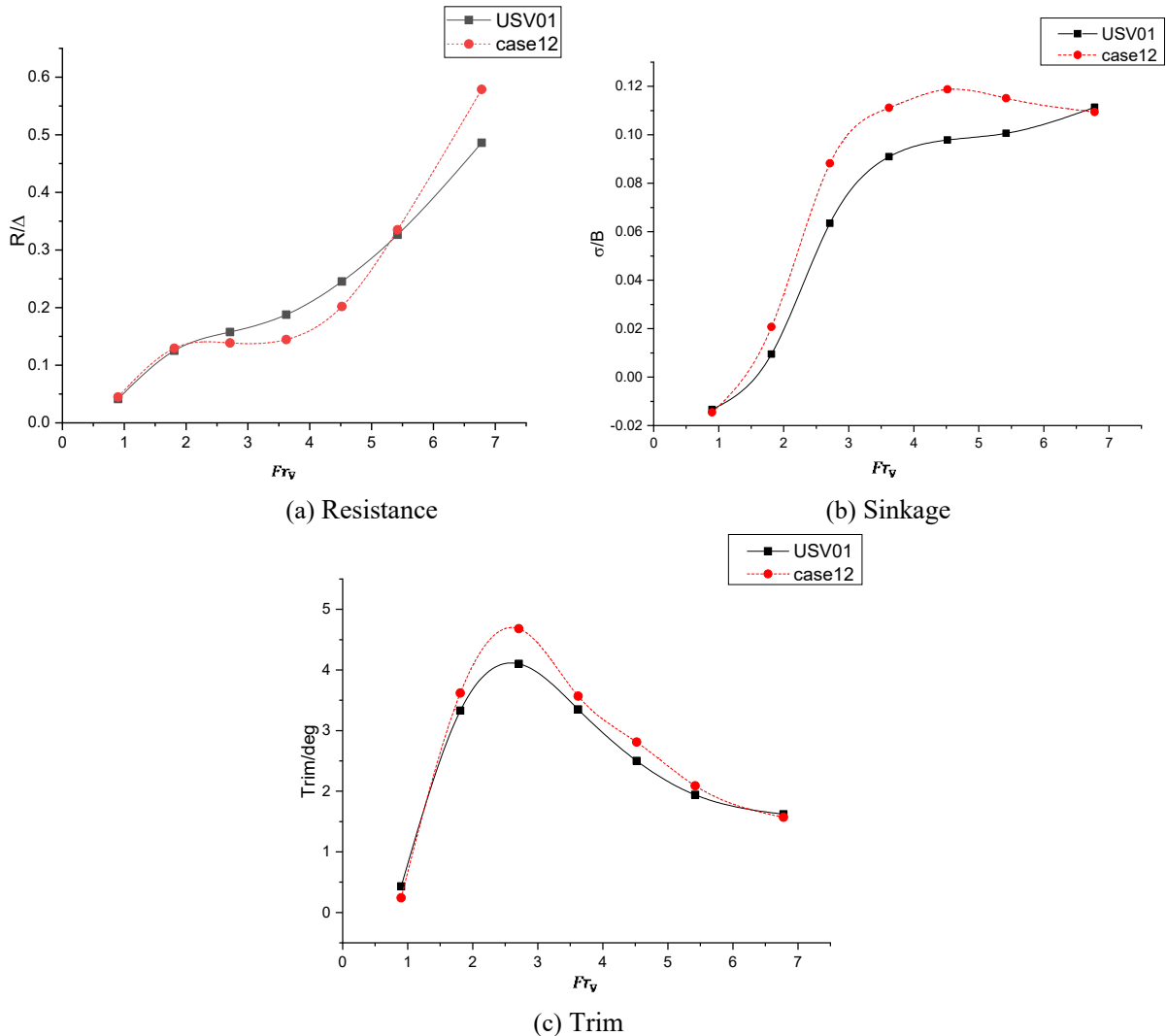
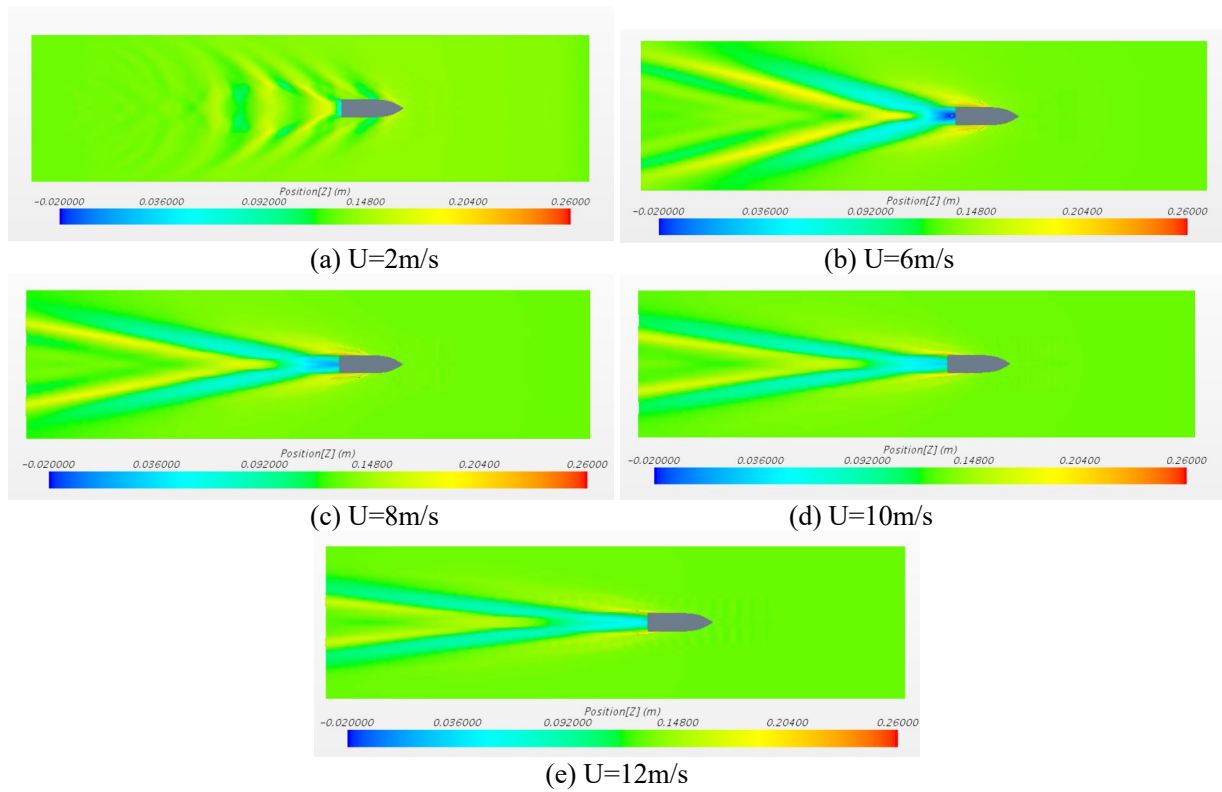


Fig. 22. Comparing resistance and sailing states at different speeds between USV01 and case12

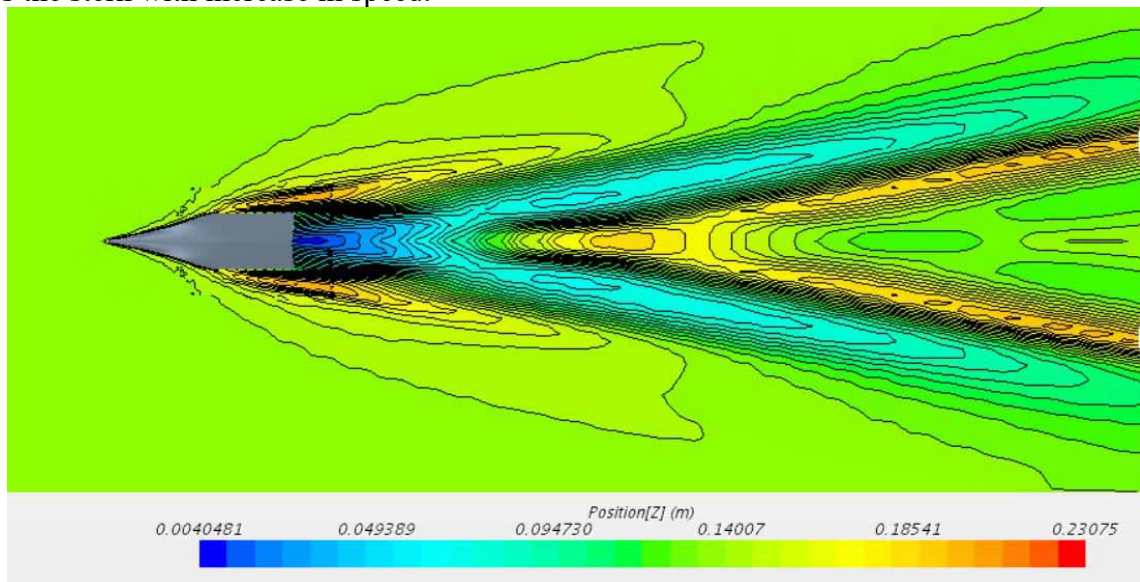
#### 4.5.4 The influence of Case 12 hydrofoil on the flow field at different speeds

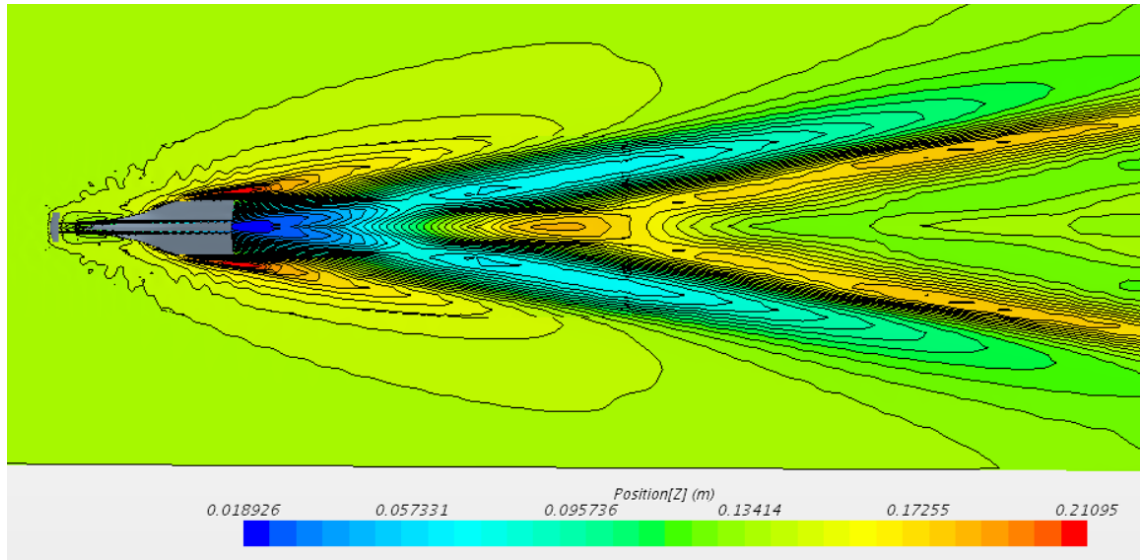
In addition to the hydrodynamic performance, the flow field around the vessel is also the key point to analyze the hydrofoil action principle, the flow field around USV01 were numerical simulated and presented in Fig. 23.



**Fig. 23.** Flow field around USV01

Fig. 23 present the variation tendency of the wake and flow field of USV01 with the increasing speed. It can be seen that the distance between the separation point of the wake field and the trailing edge increases with the increase of the speed, and the Kelvin angle of the wake flow also decreases with the increase of the speed. This indicates that with the increase of speed, the wake flow becomes more difficult to separate. Meanwhile, the proportion of shear wave in the wake decreases, while the proportion of Kelvin wave increases, and the direction of flow field around the boat body converges towards the stern with increase in speed.





(b) Case12

**Fig. 24.** Comparison of Flow field between USV01 and case12 at U=8m/s

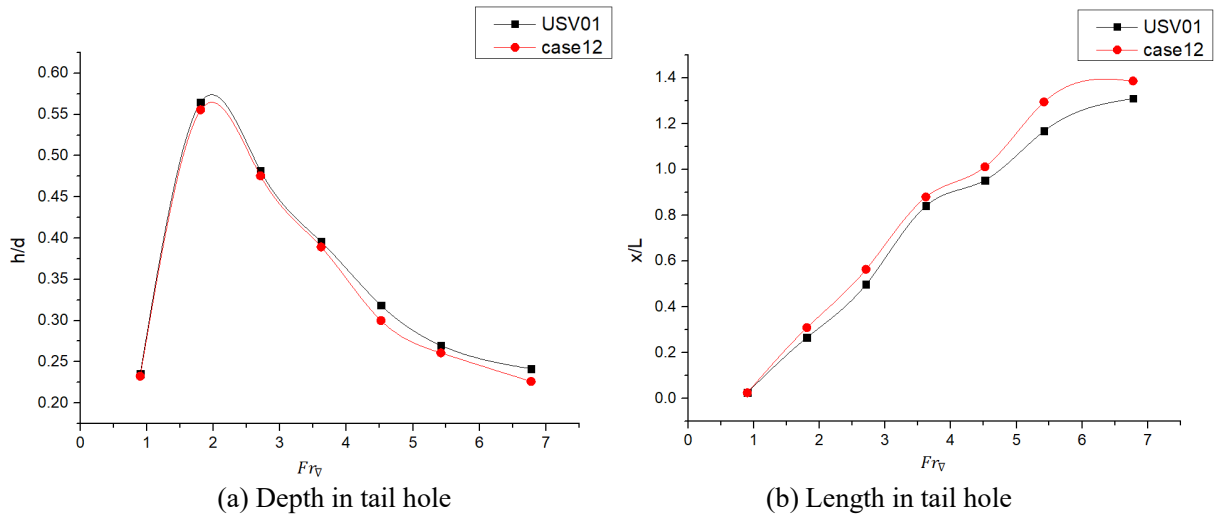
When  $U=8\text{m/s}$ , hydrofoils have the most obvious influence on the attitude of a planing boat. From Fig.24 case12 and USV01 exhibit similar circumferential flow fields during navigation. This is because the the change of attitude (heave and pitch) of the Case12 is not enough to change the circumferential flow fields of the vessel obviously.

Although the circumferential flow field remained unchanged, due to the influence of Case12 on the attitude of the vessel, the size of the hole at the stern was pronounced. The position of the separation point of the wake field from the trailing edge is directly related to location of the wave crest of the first wave in the wake flow. The hole size between the stern and the wave crest changes accordingly. The hole length is the longitudinal distance between the stern edge and the first wave crest while the hole depth is the vertical distance between the stern edge and the free liquid surface. Table 11 and Fig.25 shows the change in hole length and hole depth with speed. The length and depth of the hole were made dimensionless using hull length ( $L$ ) and depth ( $d$ ) respectively.

**Table 11.**

Depth and length in the tail hole

U(m/s)	$Fr_V$	Depth in tail hole(m)		Length in tail hole(m)	
		USV01	Case12	USV01	Case12
2	0.9	0.0765	0.0755	0.068	0.067
4	1.81	0.1835	0.181	0.730	0.85
6	2.71	0.1565	0.155	1.370	1.55
8	3.62	0.1285	0.127	2.310	2.42
10	4.52	0.1035	0.098	2.620	2.78
12	5.42	0.0877	0.085	3.210	3.56
15	6.78	0.0785	0.074	3.600	3.81

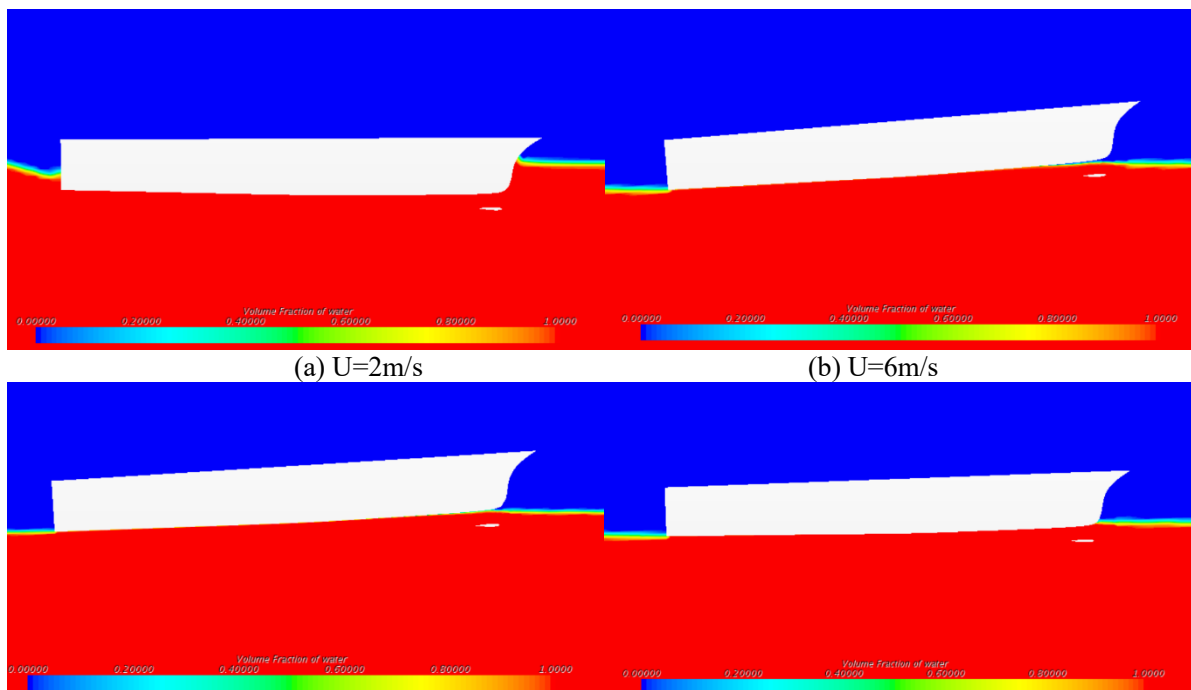


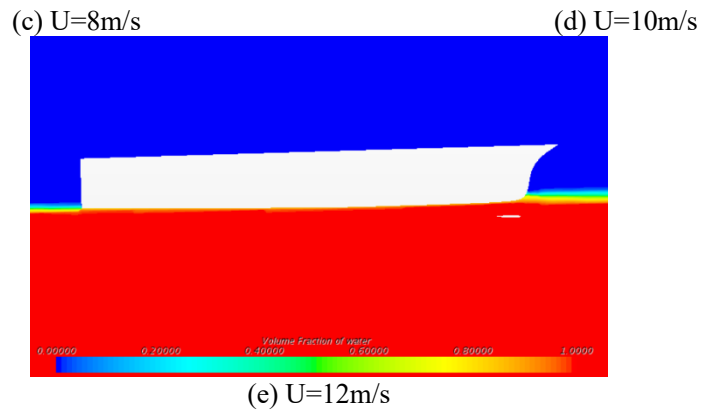
**Fig. 25** The variational tendency of the size of tail hole

Fig. 25 demonstrates that length in tail hole increases with the increase in speed. On the other hand, the depth first increases sharply to the maximum at about  $Fr=2$  and then decreases gradually. The maximum length is  $1.4L$  occurring at  $U=15\text{m/s}$  while the maximum depth is  $0.57d$  at  $U=4\text{m/s}$ . The variation tendency of depth in tail hole with speed is consistent with the trim indication that trim is the major determinant of the hole depth. Meanwhile, the increase in speed causes the first transverse wave of the chicken's wake to move sharply backward thus increasing the length in tail hole.

The size of the tail hole for Case12 becomes longer and shallower compared with USV01. This is because the hydrofoil increases the trim angle of the planing hull at all conditions. Consequently, the distance between fluid separation point and stern increases slightly making the tail hole slightly longer. However, these do not change the tendency of tail hole size with speed.

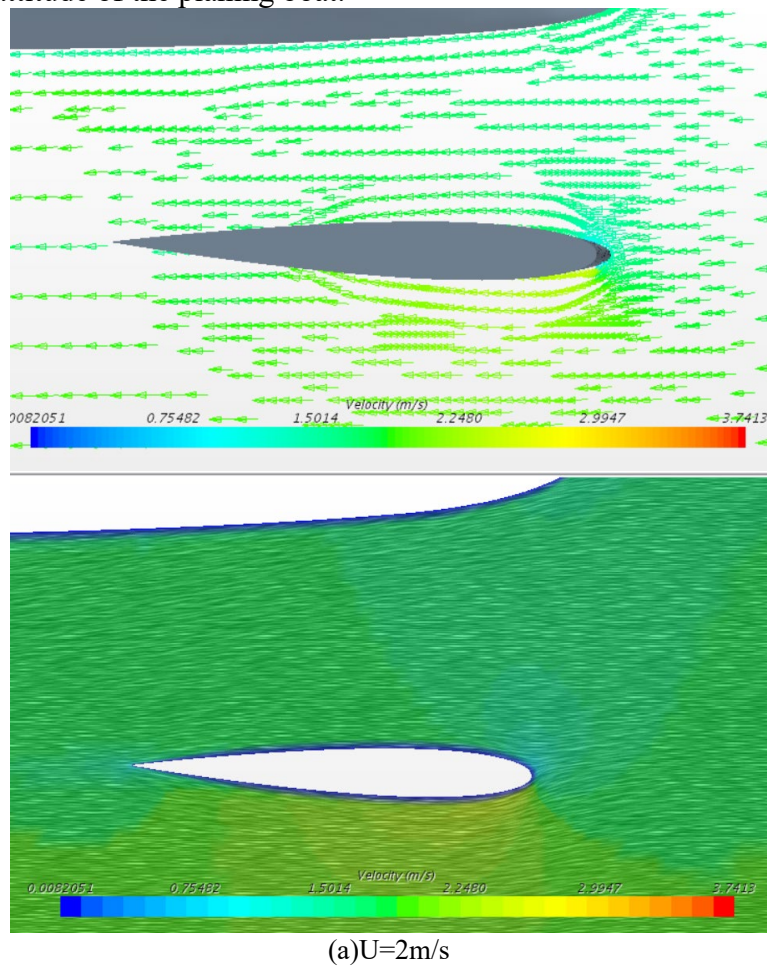
In order to further analyze the working principle of fixed hydrofoil, the numerical simulation of Case12 under the typical operating conditions of  $U=2\text{m/s}$  (drainage state),  $6\text{m/s}$  (transition state),  $8\text{m/s}$  (sliding state) and  $12\text{m/s}$  (high-speed condition) were carried out. The tendency of the flow field around the hydrofoil was then analyzed. Fig.26 presented gas-liquid two-term diagram of planing boat with case12 at different speeds.

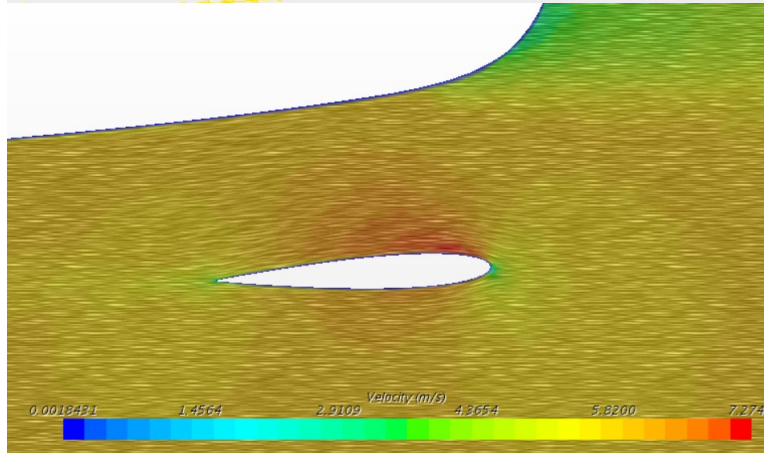
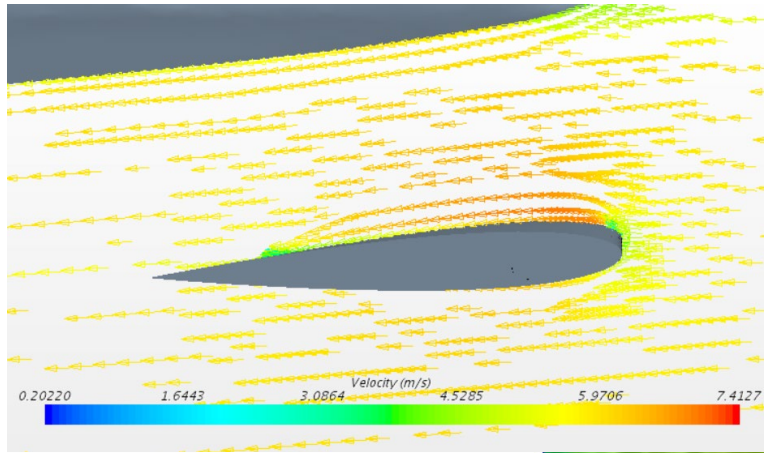




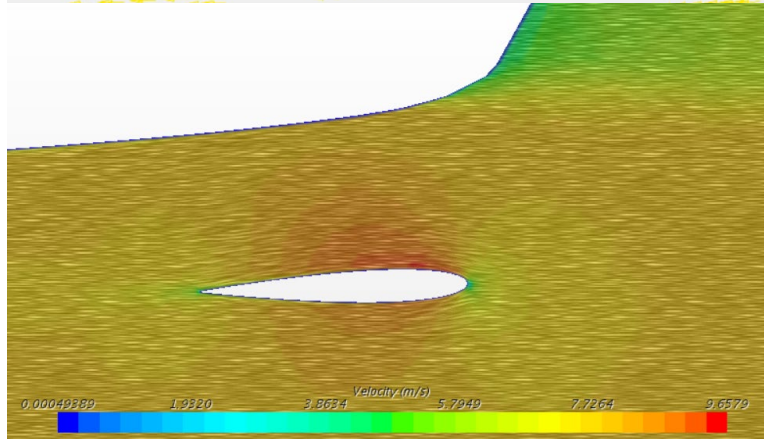
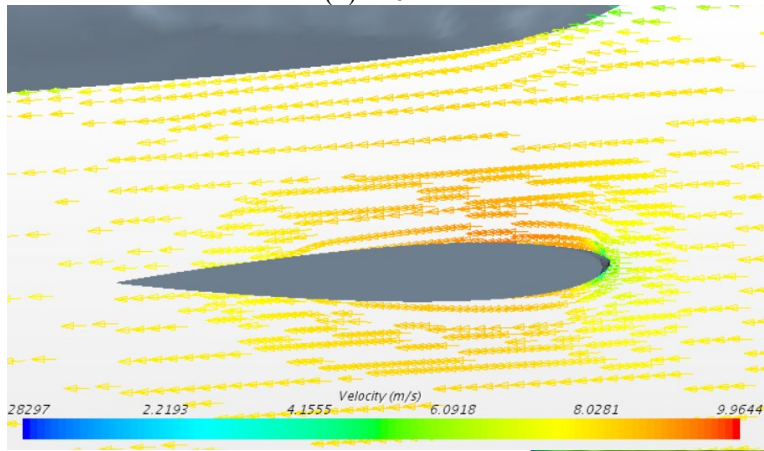
**Fig. 26.** Gas-liquid two-term diagram of planing boat at different speeds

As observed from Fig. 26, the hydrofoil case12 is  $0.65d(0.086\text{m})$  from the bottom of the bow, the hydrofoil guaranteed to stay below the free surface at all speeds, even in the condition that the trim angle reach maxium value in  $U=6\text{m/s}$ . This indicates that the influence of hydrofoils on the hull is not affected by the attitude of the planing boat.

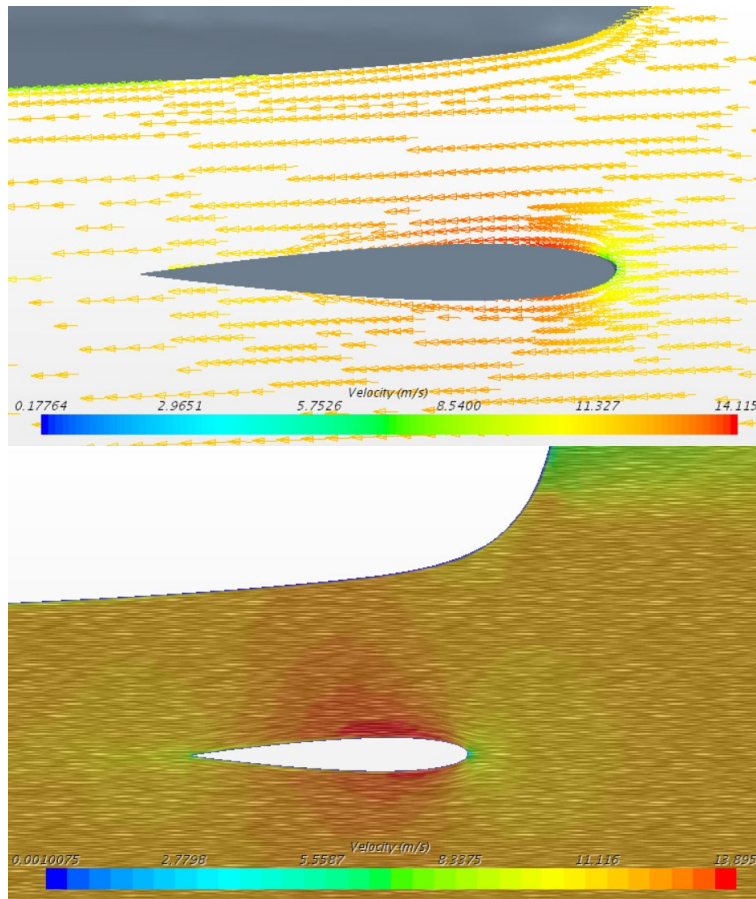




(b)U=6m/s



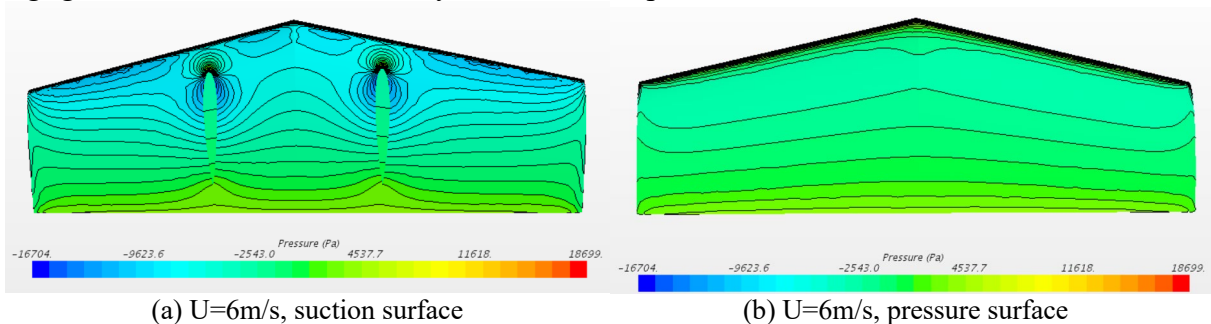
(c)U=8m/s



(d)  $U=12\text{m/s}$

**Fig. 27** The velocity field around the hydrofoil

To get a clear picture on the influence of the hydrofoil on fluid flow, the velocity field around the fixed hydrofoil and hull are presented as shown in the Fig. 27. It is seen that the velocity peak values on the suction surface is greater than the pressure surface. The water velocity difference between the suction and pressure hydrofoil surface is gradually expanded with the increasing of speed was expected. According to Bernoulli principle, the difference in flow rate generates pressure difference which acts on the center of gravity of the hull producing a trim moment. This leads to a change in the planing boat in the sailing in calm water, trim of stern of vessel is intensified, and the wet area of the hull decrease, and finally achieving resistance reduction. At the same time, the design of fixed hydrofoil affects the resistance reduction effect. The negative installation angle can increase the flow velocity difference around the hydrofoil surfaces, A larger surface. Larger surface area allows the hydrofoil to provide more lift under the same pressure difference while the design of the hydrofoil away from the main hull can increase the trim moment. Moreover, when the hydrofoil is installed away from the bottom of hull, the influence of hydrofoil on the flow field is limited to the vicinity of the hydrofoil surface. Because of this, the change trend and continuity of the flow field near the hull is negligible, which means that the hydrofoils would pose minimal disturbance to the vessel.



(a)  $U=6\text{m/s}$ , suction surface

(b)  $U=6\text{m/s}$ , pressure surface

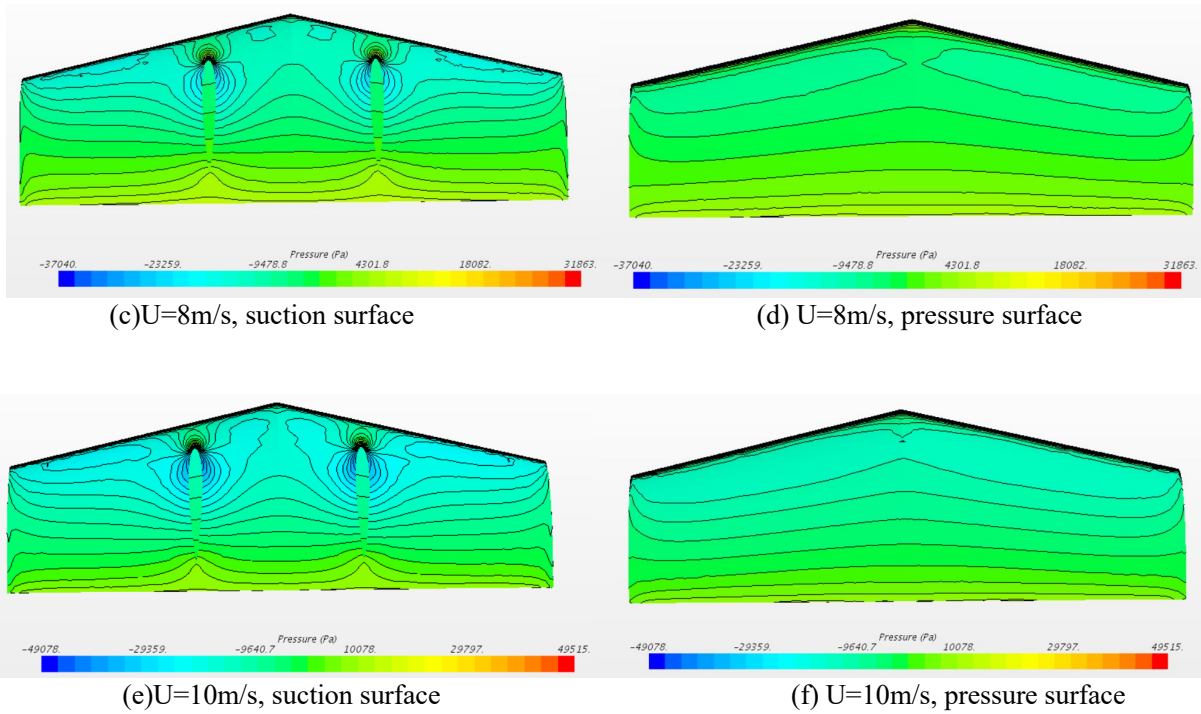


**Fig. 28** The pressure nephogram of surface of hydrofoil

As presented in Fig. 28, the pressure nephogram of surface of hydrofoil indicates that the area where pressure is most concentrated on the hydrofoil surface is the front end of the hydrofoil, at the same time, the installation strut also causes a small range of stress concentration between the hydrofoil and the strut. Due to negative attack angle, the peak value of pressure at the back of the hydrofoil is slightly higher than the pressure at the front. Meanwhile, the peak value of pressure and pressure difference on hydrofoil surface increase with the speed of the vessel. But the effect of speed on pressure distribution is not obvious.

## 5. Conclusions

This paper studied the numerical prediction method for planing boats in calm water based on CFD code STARCCM+. A simple prismatic planing model was predicted by using the numerical calculation method obtained in this paper, the resistance error was 0.23%; a real complex planing model is predicted, the maximum resistance error was 3.6%.

When the hydrofoil was fixed at a position that the distance from the stern was  $7/8$  times the length of the boat, the hydrofoils designed in this paper all had a significant resistance reduction effect at the boat design speed of  $8\text{m/s}$ . The maximum reduction of resistance was 30.74% of the total resistance of the bare planing boat at design speed of  $8\text{m/s}$ .

In the current research results, after installing the hydrofoil, the planing boat had a significant resistance reduction effect within the speed range of the real boat speed of 23.33 to 38.87 knots. When the speeds were less than 15.55kn or greater than 46.65kn, the hydrofoils would increase the resistance of the planing boat. The increase was most significant at 58.32 knots where the added resistance rose by about 19.09% of the bare boat total resistance.

The hydrofoil does not significantly change the flow field around the hull, but as the attitude of the vessel with hydrofoil changes, the size of the tail hole of vessel becomes longer and shallower compared with the bare one. The results show that the pressure difference on the hydrofoil surface is caused by the change in the velocity of the flow field, and the effect of speed is obvious.

## Acknowledgements

This research was supported by the China Scholarship Council under the project of 201706685014 and Research Fund from Science and Technology on Underwater Vehicle Technology Laboratory 2021JCJQ-SYSJJ-LB06913.

## References

- Daniel Savitsky, 1964. Hydrodynamic analysis of planing hulls. *SNAMEMar. Technol.*, 71–95.
- Clement, E.P., Blount, D.L., 1963. Resistance tests of a systematic series of planing hull forms. In: *Proceedings of SNAME Annual Meeting*, New York, NY, November, 14–15, 491–579.
- Reza Yousefi, Rouzbeh Shafaghat, Mostafa Shakeri, 2013. Hydrodynamic analysis techniques for high-speed planing hulls. *Applied Ocean Research*, 42, 105–113.
- H. Ghassemi, S. Yu-min, 2008. Determining the hydrodynamic forces on a planing hull in steady motion. *J. Mar. Sci. Appl.* 7, 147–156.
- A.R. Kohansal, H. Ghassemi, M. Ghaisi, 2010. Hydrodynamic characteristics of high speed planing hulls, including trim effects. *Turk. J. Eng. Environ. Sci.* 34, 155–170.
- A.R. Kohansal, H. Ghassemi, 2010. A numerical modeling of hydrodynamic characteristics of various planing hull forms. *Ocean Eng.* 37, 498–510.
- K.I. Matveev, 2014. Hydrodynamic modeling of planing hulls with twist and negative deadrise. *Ocean Eng.* 82, 14–19.
- K.I. Matveev, 2015. Hydrodynamic modeling of semi-planing hulls with air cavities. *Int. J. Naval Arch. Ocean Eng.* 7, 500–508.
- S.M. Mousaviraad, Z. Wang, F. Stern, 2015. URANS studies of hydrodynamic performance and slamming loads on high-speed planing hulls in calm water and waves for deep and shallow conditions. *Appl. Ocean Res.* 51, 222–240.
- P. Lotfi, M. Ashrafizaadeh, R.K. Esfahan, 2015. Numerical investigation of a stepped planing hull in calm water. *Ocean Eng.* 94, 103–110.
- S.T.G. Veysi, M. Bakhtiari, H. Ghassemi, M. Ghiasi, 2015. Toward numerical modeling of the stepped and non-stepped planing hull. *J. Braz. Soc. Mech. Sci. Eng.* 37, 1635–1645.
- Brizzolara, S., Serra, F., 2011. Accuracy of CFD Codes in the Prediction of Planing Surface Hydrodynamic Characteristics. *INSEAN (Italian Ship Model Basin)*, Rome, 147–158.
- Jahanbakhsh, E., Panahi, R., Seif, M.S., 2009. Catamaran motion simulation based on moving grid technique. *Journal of Marine Science and Technology*, Vol. 17, No. 2, 128–136.
- Seif, M.S., Jahanbakhsh, E., Panahi, R., Karimi, M.H., 2009. A unified computational method for simulating dynamic behavior of planing vessels. *China Ocean Eng.* 23(3), 517–528.
- Senocak, I., Iaccarino, G., 2005. Progress towards RANS simulation of free-surface flow around modern ships. *Center for Turbulence Research, Stanford University, Stanford, CA*, pp. 151–156.
- Yi Jiang, Hanbing Sun, Jin Zou, Ankang Hu, Jinglei Yang, 2017. Experimental and numerical investigations on hydrodynamic and aerodynamic characteristics of the tunnel of planing trimaran. *Applied Ocean Research*, 63, 1–10.
- H.K. Moghadam, R. Shafaghat, R. Yousefi, 2015. Numerical investigation of the tunnel aperture on drag reduction in a high-speed tunneled planing hull. *J. Braz. Soc. Mech. Sci.* 37, 1–12.
- Hosseini A, Tavakoli S, Dashtimanesh A, et al. Performance prediction of a hard-chine planing hull by employing different cfd models[J]. *Journal of Marine Science and Engineering*, 2021, 9(5): 481.
- Tavakoli S, Bilandi R N, Mancini S, et al. Dynamic of a planing hull in regular waves: Comparison of experimental, numerical and mathematical methods[J]. *Ocean Engineering*, 2020, 217: 107959.

- Agostino De Marco, Simone Mancini, Salvatore Miranda, Raffaele Scognamiglio, Luigi Vitiello, 2017. Experimental and numerical hydrodynamic analysis of a stepped planing hull. *Applied Ocean Research* 64,135–154.
- P. Lotfi, M. Ashrafizaadeh, R.K. Esfahan, 2015. Numerical investigation of a stepped planing hull in calm water, *Ocean Eng.* 94, 103–110.
- Bilandi R N, Dashtimanesh A, Tavakoli S. Hydrodynamic study of heeled double-stepped planing hulls using CFD and 2D+ T method[J]. *Ocean Engineering*, 2020, 196: 106813.
- Bilandi R N, Tavakoli S, Dashtimanesh A. Seakeeping of double-stepped planing hulls[J]. *Ocean Engineering*, 2021, 236: 109475.
- Larsson, L., Eliasson, R.E., Orych, M., 2014. *Principles of Yacht Design*, fourth ed. Adlard Coles Nautical, London.
- S. Bal, S. Kinnas, 2003. A numerical wave tank model for cavitating hydrofoils, *Comput. Mech.* 32, 259–268.
- S. Bal, 2007. High-speed submerged and surface piercing cavitating hydrofoils, including tandem case, Volume 34, Issues 14–15, 1935-1946.
- Clement, E.P., 1964. Effects of Longitudinal Bottom Spray Strips on Planing Boat Resistance. DTMB Report, No.1818. David Taylor Model Basin, Washington, DC.
- Lee, K., Park, N. and Lee, E., 2005. An experimental study on the improvement of resistance performance by appendage for 50knots class planing hull form. *Bulletin of the Korean Society of Fisheries Technology*, 41(3), 222-226.
- D. Savitsky, M. Morabito, 2010. Surface wave contours associated with the fore body wake of stepped planing hulls, *Mar. Technol.* 47 ,1–16.
- K.I. Matveev, 2012. Two-dimensional modeling of stepped planing hulls with open and pressurized air cavities, *Int. J. Naval Archit. Ocean Eng.* 4 (2), 162–171.
- P. Lotfi, M. Ashrafizaadeh, R.K. Esfahan, 2015. Numerical investigation of a stepped planing hull in calm water, *Ocean Eng.* 94, 103–110.
- Migeotte G . Development of hydrofoil supported catamarans with semi-displacement hulls[J]. Stellenbosch Stellenbosch University, 1997.
- Chi Yunpeng, Mng Xianqing. Experimental study on resistance and seakeeping of high speed channel boat. *Ship Engineering*. 1995(3):27-31.
- Chi Yunpeng, Wang Shaoxin, Meng Xianqin, Zhao Zhiping. Investigation of resistance performance test for channel planing craft with hydrofoils. *ournal of Dalian University of Technology*. 1996(4):466-470.
- Sclavounos P D, Borgen H. Seakeeping Analysis of a High-Speed Monohull With a Motion-Control Bow Hydrofoil[J]. *Journal of Ship Research*, 2004.
- Budiyanto M A, Syahrudin M F , Murdianto M A . Investigation of the effectiveness of a stern foil on a patrol boat by experiment and simulation[J]. *Cogent Engineering*, 2020, 7(1).
- Budiyanto M A, Wibowo H T, Naufal F, et al. Study on the effectiveness of a stern-foil on a multi-chine hulls[C]. *IOP Conference Series: Materials Science and Engineering*. IOP Publishing, 2021, 1034(1): 012064.
- Azis D N, Chrismianto D, Adietya B A. Analisa Gaya Angkat dan Hambatan pada Dihedral Surface Piercing Hydrofoil Katamaran Menggunakan Metode CFD (Computational Fluid Dynamic)[J]. *Jurnal Teknik Perkapalan*, 2019, 7(4).

- Dwiputera H, Prawira N Y, Budiyanto M A, et al. Effect of Angle of Attack Variation of Stern Foil on High-Speed Craft on Various Speed with Computational Fluid Dynamics Method[J]. *International Journal of Technology*, 2020, 11(7): 1359-1369.
- Hou H, Krajewski M, Ilter Y K, et al. An experimental investigation of the impact of retrofitting an underwater stern foil on the resistance and motion[J]. *Ocean Engineering*, 2020, 205: 107290.
- Ismail I N, Manik P, Indriyanto M. Effect of the Addition of Hydrofoil on Lift Force and Resistance in 60 M High-Speed Vessel[J]. *Kapal: Jurnal Ilmu Pengetahuan dan Teknologi Kelautan*, 17(3): 95-106.
- Wang, S., Su, Y., Wang, Z., Zhu, X., & Liu, H., 2014. Numerical and experimental analyses of transverse static stability loss of planing craft sailing at high forward speed. *Engineering Applications of Computational Fluid Mechanics*, 8(1), 44-54.
- Jiang, Y., Sun, H., Zou, J., Hu, A., & Yang, J., 2017. Experimental and numerical investigations on hydrodynamic and aerodynamic characteristics of the tunnel of planing trimaran. *Applied Ocean Research*, 63, 1-10.
- Marco, A., Mancini, S., Miranda, S. Scognamiglio, R., & Vitiello, L., 2017. Experimental and numerical hydrodynamic analysis of a stepped planing hull. *Applied Ocean Research*, 64, 135-154.
- J. Blazek, 2005. *Computational Fluid Dynamics: Principles and applications*, Second Edition, Published by Elsevier, Ltd., Amsterdam, The Netherlands, 225-256.
- David C. Wilcox, 1994. "Turbulence energy equation models," in *Turbulence modeling for CFD*. vol. I, California: DCW Industries, Inc., 73-163.
- David C. Wilcox, 2008. "Formulation of the k-omega turbulence model revisited," *AIAA Journal*, vol. 46, 2823-2838.
- SAVITSKY D., 1951. Wetted length and center of pressure of vee-step planing surfaces. Experimental Towing Tank Stevens Institute of Technology, Prepared Under Contract with U.S. Navy Office of Naval Research Project NO. NR 062-012, Report NO. 378.
- ITTC, 2011. Recommended Procedures and Guidelines Practical Guidelines for Ship CFD Applications 7.5-03-02-03, 1-18.
- Siemens PLM Software, 2017. STAR- CCM+ User Guide, Version 12.04
- Liang Zhang, Yunbo Li, 2001. *Fluid dynamics*. Published by Harbin Engineering University Press, Harbin, China.
- Hailong Shen, Debo Huang, 2011. 2.75m ship resistance test report. No. 2.75MCM-SDSY-11-07-16-003. China Institute of Special Vehicles High-speed Hydrodynamic Laboratory Basin, Jing Men, China.
- ITTC, Recommended Procedures and Guidelines 7.5-02-02-01. 2017. <https://www.ittc.info/media/8001/75-02-02-01.pdf>
- Bi X, Shen H, Zhou J, et al. Numerical analysis of the influence of fixed hydrofoil installation position on seakeeping of the planing craft[J]. *Applied Ocean Research*, 2019, 90:101863.